ACCSCIENCE PUBLISHING

International Journal of Bioprinting

RESEARCH ARTICLE

3D-bioprinted model of adult neural stem cell microenvironment in Alzheimer's disease

Natalia Dall'Agnol Ferreira[1,2], Paula Scanavez Ferreira[1,2], Cristina Pacheco Soares[3], Marimelia Aparecida Porcionatto[1,2*], and Geisa Rodrigues Salles[1,2,3*]

[1] Department of Biochemistry, Escola Paulista de Medicina, Universidade Federal de São Paulo, São Paulo, Brazil

[2] National Institute of Science and Technology in Modeling Human Complex Diseases with 3D Platforms (INCT Model 3D), São Paulo, Brazil

[3] Research & Development Institute, Universidade do Vale do Paraíba, São José dos Campos, São Paulo, Brazil

(This article belongs to the *Special Issue: Innovative Tissue and Diseases Models – Novelties in Bioprinting/3D bioprinting*)

Abstract

Neurogenesis plays a major role in neuroplasticity and memory. In adult human and mouse brains, neural stem cells (NSCs) are mainly distributed in two extensively characterized neurogenic niches: the subgranular zone (SGZ) of the hippocampus and the subventricular zone (SVZ) of the lateral ventricles. Impaired neurogenesis is one of the consequences of Alzheimer's disease (AD), contributing to cognitive decline and progressive memory loss. Developing new *in vitro* models that resemble this three-dimensional (3D) structure is fundamental for enhancing our understanding of the SVZ neurogenic niche dynamics in AD. Herein, we produced and characterized a 3D-bioprinted model of the adult SVZ neurogenic niche containing amyloid β (Aβ) oligomers, mimicking the NSC microenvironment in AD. In this model, Aβ oligomers induce oxidative stress and reduce the proliferative potential of NSCs, while stimulating neuronal differentiation. We hypothesize that these events are an early attempt of adult NSCs to compensate for neuronal death in AD pathogenesis. Our 3D model simulates the NSC niche physiology, reproducing an early response of NSCs in AD, strengthening the importance of studying the potential of neurogenesis in neurodegeneration.

Keywords: Bioprinting; Neurogenic niche; Alzheimer's disease; Amyloid beta; Neural stem cells; Subventricular zone

***Corresponding authors:**
Marimelia Aparecida Porcionatto (marimelia.porcionatto@unifesp.br)

Geisa Rodrigues Salles (geisa.salles@unifesp.br)

Citation: Ferreira NDA, Ferreira PS, Soares CP, Porcionatto MA, Salles GR. 3D-bioprinted model of adult neural stem cell microenvironment in Alzheimer's disease. *Int J Bioprint*. 2024;10(5):3751. doi: 10.36922/ijb.3751

Received: May 24, 2024
Accepted: July 19, 2024
Published Online: September 13, 2024

1. Introduction

Neurogenesis is defined as the process of generating neurons from neural stem cells (NSCs). In the adult brain, neurogenesis confers plasticity and neuronal replacement and occurs primarily in specialized regions known as neurogenic niches. The two main neurogenic niches of human and mouse brains are located in the subgranular zone (SGZ) of the hippocampus and the subventricular zone (SVZ) of lateral ventricles. As

the hippocampus is involved in memory and learning,[1] most studies involving neurogenesis in Alzheimer's disease (AD) primarily focus on this niche,[2–5] noting that neurogenesis decreases mainly due to amyloid beta (Aβ) aggregation and senile plaque formation.

However, recent studies have demonstrated that alterations in adult SVZ neurogenesis also play a crucial role in AD.[6–10] Transplantation of SVZ-derived newborn neurons can restore impaired neural circuits, which compensates for the reduced neuronal population found in AD,[11] playing a pivotal role in cognitive function and disease pathogenesis. Moreover, by undefined pathways, neurogenesis in the SVZ may be regulated and stimulated by Aβ in young adult animals.[12] Despite all evidence, there is a lack of studies focusing on the role of adult SVZ neurogenesis in AD.

The contribution of Aβ to AD initiation and progression is highly complex; it participates in different cellular events depending on the peptide's aggregation state, concentration, and the brain's developmental stage. Aβ can either impair the brain's homeostatic balance, as in AD, or play a role in normal brain development, by inducing NSC self-renewal and differentiation into neurons, astrocytes, and oligodendrocytes.[13] Aβ peptides are generated by enzymatic cleavage of amyloid precursor protein (APP) in the plasma membrane of neurons and glial cells. Two distinct pathways lead to APP cleavage: (i) the non-amyloidogenic pathway that results in the formation of a soluble form of APP (sAPPα), and (ii) the amyloidogenic pathway, which results in the formation of Aβ peptides that can form insoluble aggregates, a hallmark of AD. In the amyloidogenic pathway, APP is cleaved in distinct positions by two secretases (β and γ), producing different sizes of Aβ ($Aβ_{40}$ and $Aβ_{42}$), where $Aβ_{42}$ has more significant aggregation potential, resulting in senile plaques. Consequently, oxidative stress is observed during the formation of these plaques, inducing inflammatory responses, which enhances the aggregation of Aβ peptides and impairs synaptic plasticity.

As the brain is distinctly dynamic, the complexity of NSCs and Aβ oligomer interactions demands investigating AD using novel strategic models. Biotechnology and bioengineering have much to contribute, especially providing tools to develop biomaterials that may increase knowledge of pathophysiological mechanisms of the disease, in addition to reducing the number of animals used and highlighting specific pathways to be studied. Recently, valuable attention has been directed toward 3D models,[14–16] which create dynamic microenvironments that mimic the complexity of various tissues, including the brain.

Bioprinting has emerged as a highly promising tool for neurobiology, offering a technological approach to tailor 3D constructs effectively.[17–19] Moreover, bioprinting enables the creation of volumetric, biomimetic microenvironments that can emulate specific events of the central nervous system (CNS).[20] By designing specific combinations of cells and hydrogel that mimic the extracellular matrix environment, neurogenic niches, and other areas of the brain, specific microstructures can be potentially bioprinted.[17,21–25]

Therefore, bioprinting is at the forefront of elucidating NSC behavior by studying distinct areas, such as retina recreation by stem cell transplantation;[26] toxicological performance of compounds, such as cannabidiol, on neuroprogenitor cells;[27] modeling neural tissue using induced pluripotent stem cells (iPSCs) and iPSC-derived NSCs;[28] evaluation of neural regeneration;[29] and recapitulating areas of damaged CNS tissue.[30]

Although this technological tool is very promising, there is a lack of studies involving modeling and bioprinting neurodegenerative conditions, especially reproducing and biomimicking NSCs in AD. In this study, we developed and characterized a 3D model of the adult SVZ-NSC environment in AD by bioprinting NSC-derived neurospheres from six-week-old wild-type mice in a bioink containing Aβ oligomers. The biomaterial we produced and standardized may serve as a platform to further develop novel therapeutic strategies, also contributing to providing greater insights into underlying disease mechanisms.

2. Materials and methods

2.1. Study design

This study was designed to develop a 3D model of the adult SVZ-NSC microenvironment, representing a brain area, aside from the hippocampus, that can be a target for early events of neurodegeneration in AD. Briefly, SVZ-derived NSCs were isolated from six-week-old C57BL/6 mice, cultured as neurospheres, and bioprinted with or without $Aβ_{1–42}$ oligomers in the bioink composition. The constructs' physicochemical properties were characterized; the neurosphere areas were measured; and cell proliferation, oxidative stress, and cell differentiation were quantified.

2.2. Reagents and equipment

All reagents and equipment used in this work are described in Table 1.

2.3. Preparation of the hydrogel

The hydrogel (the polymeric base of the bioink) was composed of a homogenized combination of low-viscosity sodium alginate (ALG; molecular weight [M_W]: 30–100 kDa) and gelatin (GEL; M_W: ~ 50–100 kDa; type A from

Table 1. Reagents and equipment.

Reagent Or Resource	Source	Identifier
Reagents, antibodies, supplements, and other chemicals		
Accutase	Gibco, USA	A1110501
Alexa Fluor 488 Goat anti-Rabbit	Invitrogen, USA	A11008
Alexa Fluor 647 Goat anti-Chicken	Invitrogen, USA	A21449
Aβ-protein (Human, $A\beta_{1-42}$)	Peptide Institute, INC, Japan	4349-v
B-27 Supplement Minus Vitamin A	Gibco, USA	12587010
Calcium Chloride ($CaCl_2$)	Synth, Brazil	C201301AH
CellROX (Green Reagent)	Invitrogen, USA	C10444
DAPI	Sigma-Aldrich, USA	62248
Dimethyl sulfoxide (DMSO)	Sigma-Aldrich, USA	1003246030
Dulbecco's modified eagle medium/Nutrient mixture F-12 (DMEM/F12)	Gibco, USA	12400024
Fetal Bovine Serum (FBS)	Gibco, USA	12657-029
Gelatin from porcine skin (GEL)	Sigma-Aldrich, USA	G2500, 9000-70-8
Bovine sodium heparin	Kin Master, Brazil	50.1000.01
Human FGF-basic (FGF-2/bFGF)	Gibco, USA	PHG0026
L-glutamine	MP Biomedicals, USA	101806
LIVE/DEAD assay (Cell Imaging Kit 488/570)	Invitrogen, USA	R37601
Penicillin/streptomycin	Gibco, USA	15140-122
Phalloidin	Sigma-Aldrich, USA	49409
poly (2-hydroxyethylmethacrylate) (poly-hema)	Sigma-Aldrich, USA	P3932
Primary MAP-2 Antibody (Rb X MAP2)	Sigma-Aldrich, USA	ab5622
Primary Nestin Antibody (Chk pAb to Nestin)	Abcam, USA	ab134017
Recombinant Human EGF Protein	R&D System, USA	236-EG-01M
Resazurin powder	Sigma-Aldrich, USA	R7017
Sodium alginate (ALG, Alginic acid sodium salt from brown algae)	Sigma-Aldrich, Norway	A1112
Triton X-100	Sigma-Aldrich, USA	9002-93-1
Trypsin	Gibco, USA	15090046

Reagent Or Resource	Source	Identifier
Plastics and other non-perishable materials		
Cell culture dishes (100 mm)	Biofil, Brazil	TCD 000100
Cell culture flasks (25 cm^2 and 75 cm^2)	Corning, USA	430168
Cell culture plates (24 well)	Costar, USA	3524
Cell strainer (40μm nylon)	Falcon, USA	352340
Needles (25x0.70/0.60 22 G 1)	Injex, Brazil	25x0.70/0.60 22 G 1
Polypropylene conical tubes (15 mL and 50 mL)	Falcon, USA	352070 and 352095
Serological pipettes (1, 5, 10, and 25 mL)	Biofil, Brazil	GSP-010-005
Syringes (5 mL)	Descarpack, Brazil	
Equipment and Softwares		
3D Bioprinter	3D Biotechnology Solutions, Brazil (3DBS) Educational Starter, Brazil	http://www.3dbiotechnologiessolutions.com/educacional-starter/
ATR-FTIR spectrophotometer	Perkin Elmer FTIR Imaging System, USA	Spotlight-400
Centrifuge	Eppendorf, Germany	5702
Conductivity meter	Lactea, Brazil	
Confocal laser scanning microscope	Leica, Germany	TCS SP8
Electronic digital scale	Shimadzu, Brazil	AY220
Goniometer	KRUSS, Germany	EasyDrop DSA 100S
Hot plate magnetic stirrer	Kasvi, Brazil	
Humidifier incubator	Thermo Scientific, USA	Series 3 Water Jacketed
Microplate reader	Molecular Devices, USA	SpectraMax® M3
Microscope (Inverted fluorescent and phase contrast)	Olympus, USA	IX51 TH4-100
pHmeter	Kasvi, Brazil	K39-1420A
Pronterface software	Printrun, USA	Graphical User Interface host from Printrun
Rheometer	Thermo Scientific, Germany	Haake MARS 40/60
Scanning electron microscope	Zeiss, USA	EVO MA-10
Water bath	Novatecnica, Brazil	N1030T

porcine skin; and gel strength: ~300 g bloom). GEL (4% w/v) was first dissolved in sterile phosphate-buffered saline (PBS) on a hot plate magnetic stirrer at 72°C under constant agitation of 3 rcf. Once the powder was completely dissolved, ALG (6% w/v) was added to the solution and stirred for 30 min. The final solution was exposed to ultraviolet (UV) light for 30 min before printing.

2.4. Bioprinting and crosslinking the hydrogel

For bioprinting, 2 mL of the hydrogel was maintained in a water bath at 37°C, transferred to a 5 mL syringe with a 22-gauge blunt needle, and placed in the printhead of the 3D bioprinter. The bioprinting speed was set at 300 mm/min, at room temperature, and under G-code control, using two different extrusion codes in Pronterface software. The resulting constructs consisted of four deposited layers of cell-laden bioink (6 × 6 × 0.6 mm; Code 1) or six layers (6 × 6 × 1 mm; Code 2), as described in Table 2. Each construct was printed and deposited in a well of a 24-well plate, and the hydrogel was crosslinked in calcium chloride ($CaCl_2$) solution (2% w/v, diluted in distilled water, dH_2O) for 5–7 min.

2.5. Swelling degree

Constructs were weighed immediately after they were printed and crosslinked, before incubation in dH_2O or Dulbecco's modified eagle medium/nutrient mixture F-12 (DMEM/F12) (pH 7.2) at 37°C and 5% CO_2. They were weighed at different time points (0, 1, 2, 7, 14, 21, and 28 days). The percentage of swelling was calculated using **Equation I**:

$$Swelling\ (\%) = \frac{W_f - Wd_o}{Wd_o}\ x\ 100 \qquad (I)$$

where W_f is the final wet weight and Wd_o is the initial dry weight of constructs. Four constructs were weighed at each time point.

2.6. Degradation rate

The degradation rate of the constructs was determined by quantifying the weight loss of dry constructs. The printed constructs were weighed immediately after they were printed and crosslinked. They were then incubated in dH_2O or DMEM/F12 (pH 7.2) at 37°C and 5% CO_2. At different time points (0, 1, 2, 7, 14, 21, and 28 days), constructs were carefully blotted with filter paper to remove the excess liquid, maintained in a dry oven at 37°C for 20 min, and reweighed. The degradation percentage was calculated using **Equation II**:

$$Degradation\ (\%) = \frac{Wd_o - Wd_f}{Wd_o}\ x\ 100 \qquad (II)$$

Table 2. Bioprinting parameters.

Parameter	Code	
	1	2
Dimension (mm)		
X-axis	6	6
Y-axis	6	6
Z-axis	0.6	1
Number of layers	4	6
Individual layer height (mm)	0.2	0.2

where Wd_o is the initial dry weight and Wd_f is the final dry weight of constructs. Four constructs were weighed at each time point.

2.7. Wettability

The wetting of aqueous drops on the surface of constructs was characterized using a goniometer. Contact-angle measurements were based on the sessile drop method using aqueous drops at a volume of 5 µL placed on the top of the construct. Briefly, images of a single drop of deionized water deposited on the construct's surface were periodically acquired (every 2 min) by a custom setup with a charged-coupled device (CCD) camera. The first contact angle was measured 5 s after drop-casting to ensure the droplet reached equilibrium. Images were collected in triplicate, using different constructs, and contact angle values were measured. All measurements were conducted at a controlled temperature (25 ± 3°C) and humidified atmosphere (50 ± 10%).

2.8. Scanning electron microscopy

The surface observation of the constructs was performed by scanning electron microscopy (SEM). Right after crosslinking (day 0) and 14 days after dH_2O or DMEM/F12 incubation at 37°C and 5% CO_2, bioprinted constructs were dehydrated with a crescent sequence of acetone (30, 50, 70, and 100%) for 5 min in each solution. After that, samples were immersed in a 1:1 ratio of acetone: hexamethyldisilazane (HMDS) for 5 min, and finally in HMDS alone until the solution evaporated. Constructs were dried, sputter-coated with a thin layer of gold, and observed under a scanning electron microscope.

2.9. Attenuated total reflectance-Fourier transform infrared spectroscopy

The chemical structures of ALG, GEL, $CaCl_2$, crosslinked and non-crosslinked hydrogel, Aβ oligomers, and constructs with neurospheres (with and without Aβ oligomers) were analyzed using an attenuated total reflectance-Fourier transform infrared ATR-FTIR spectrophotometer at a range of 400–4000 cm^{-1} in transmittance mode.

2.10. Rheological characterization

The mechanical properties of the hydrogel were studied through rheological assessment using a stress-controlled rheometer with a parallel plate configuration (25 mm diameter; 200 μm gap). To determine the hydrogel's flow behavior and viscosity profile, samples were subjected to shear rates ranging from 0.01 to 100 s^{-1} and back with an interval of 30 s between curves. Next, oscillatory analyses were conducted to evaluate the viscoelastic properties of the hydrogels and constructs. Through amplitude sweep (1 Hz frequency; 0.1–100% strain) and frequency sweep (1% strain; 0.1–10 Hz) measurements, the values for storage modulus (G'), loss modulus (G"), and loss tangent (tan δ) were obtained. All measurements were performed at 25°C (room temperature), and each experiment was conducted in triplicate to ensure consistency. The rheograms are plotted based on the average of three replicates.

2.11. Electrical conductivity

The electrical conductivity of 5 mL of the hydrogel was determined using a conductivity meter.

2.12. Animals

All experiments using animals and their respective extracted cells were conducted with the approval of the Ethics Committee on the Use of Animals from the Universidade Federal de São Paulo (authorization number CEUA 2428100423). C57BL/6 wild-type male mice were dissected at six weeks of age. In detail, mice were divided into two groups and housed in standard cages (hardwood bedding) in a conventional animal facility (12 h light/dark cycle). Mice were monitored for health and welfare for the whole duration of the experiments. Only mice without signs of stress or discomfort (including hair loss and stereotype behaviors) were included in the study.

2.13. Neural stem cell extraction and neurosphere culture

Briefly, six-week-old mice were euthanized by decapitation, and their brains were removed. The SVZ was dissected, and cells were dissociated mechanically and enzymatically with 0.5% trypsin for 5 min at 37°C. After dissociation, cells were strained in a 40 μm mesh cell strainer and cultured in poly(2-hydroxyethylmethacrylate) (polyHEMA) pre-coated flasks, seeded in a complete medium (DMEM/F12 supplemented with 2% B-27 without vitamin A supplement, 20 ng/mL epidermal growth factor (EGF), 20 ng/mL fibroblast growth factor 2 (FGF2), 1% l-glutamine, 1% penicillin/streptomycin, and 5 μg/mL heparin) and maintained in a humidified incubator at 37°C and 5% CO_2 for three weeks. For propagation, neurospheres (100–200 μm in diameter) were subcultured by mechanical and enzymatic dissociation (described below), and the procedure was repeated on newly formed neurospheres. Half of the medium volume was replaced every 2–3 days.

2.14. Dissociation of neurospheres

Once the neurospheres reached approximately 100–200 μm in diameter, they were dissociated as follows. Briefly, cells were centrifuged at 200×g for 4 min and suspended in Accutase. Dissociation was performed mechanically and enzymatically with repeated up-and-down pipetting of neurospheres in Accutase. Then, the solution was incubated at 37°C for 10 min, and DMEM/F12 was added to the solution, which was then centrifuged at 200×g for 5 min. After discarding the supernatant, dissociated neurospheres were resuspended in the complete medium. Four days after dissociation, neurospheres were immersed into the hydrogel and bioprinted as described below.

2.15. Bioprinting the NSC microenvironment

The bioink was composed of 2×10^4 neurospheres mixed with 1 mL of the hydrogel with or without 1 μM Aβ oligomers. The bioink was transferred to a 5 mL syringe. Bioprinting and crosslinking were performed as described in **Section 2.4**. Thereafter, the constructs were transferred to 24-well plates and cultured with the complete medium at 37°C and 5% CO_2. The medium was changed every 2–3 days. Constructs were evaluated 2, 3, or 8 days after bioprinting.

2.16. Cellular proliferation and viability

The resazurin assay was used to assess cell proliferation at different time points (2, 3, and 8 days after bioprinting). Briefly, 24 h before the determined time point, the medium was substituted by 10% resazurin solution diluted in a complete medium. Samples were incubated at 37°C and 5% CO_2 for 24 h. Subsequently, the solution of each sample was transferred to a new plate for fluorescence measurement using a microplate reader (bottom-reading; excitation: 544 nm; emission: 590 nm). As a negative control, cell-free 10% resazurin solution was incubated for the same period under the same conditions. The results are presented as a percentage of the control.

To observe the distribution and localization of live and dead cells within the neurospheres cultured in the construct, viability was assessed using a Live/Dead assay kit two days after bioprinting. Constructs were incubated with a homogenized solution of calcein AM and ethidium homodimer-1 at room temperature for 15 min. Stained cells were imaged using a confocal laser scanning microscope.

2.17. Neurosphere area

On a phase contrast microscope, constructs were imaged on days 0, 1, 2, 3, 4, 7, and 8 after bioprinting. The area

of neurospheres in the constructs was measured using ImageJ software.

2.18. Morphological aspects

On day 2 after bioprinting, constructs without Aβ oligomers were fixed in 4% paraformaldehyde (PFA) and diluted in dH_2O for 40 min at room temperature. Samples were stained with phalloidin and 4′,6-diamino-2-phenylindole (DAPI) overnight and imaged using a confocal microscope to evaluate the shape and morphology of cells within the construct.

On day 3 after bioprinting, constructs were fixed in 4% PFA and diluted in dH_2O for 40 min at room temperature. Samples were dehydrated, sputter-coated with a thin layer of gold, and observed under a scanning electron microscope, as described in **Section 2.7**.

2.19. Oxidative stress

To evaluate the induction of oxidative stress, cytochemical analysis was performed using CellROX®. On days 2 and 3 after bioprinting, constructs were incubated with 5 μM CellROX® Green Reagent for 30 min at 37°C and 5% CO_2. Green fluorescent neurospheres were imaged using an inverted confocal laser scanning microscope. Fluorescence intensity quantification was performed with ImageJ software.

2.20. Cell differentiation

The differentiation of NSCs into neurons was investigated. Constructs were fixed in 4% PFA, diluted in dH_2O, and permeabilized with dH_2O-0.1% Triton X (dH_2O-T) for 5 min. After three washes, cells were incubated with blocking solution (5% fetal bovine serum in dH_2O-T) for 1 h at room temperature, followed by overnight incubation with anti-Nestin (1:250) and anti-microtubule-associated protein 2 (MAP-2) (1:500) and diluted in blocking solution at 4°C. Constructs were then washed with dH_2O and incubated overnight at 4°C with the corresponding secondary antibodies and fluorescence nuclear counterstain DAPI. Samples were imaged under an inverted confocal laser scanning microscope. Fluorescence intensity quantification was performed using ImageJ software.

2.21. Statistical analyses

Data are expressed as mean ± standard deviation. Statistical significance between groups was evaluated using one-way analysis of variance (ANOVA), followed by Bonferroni post hoc test for multiple comparisons using GraphPad Prism 5.0 (GraphPad Inc., USA). Statistical significance was set at $^{*}p < 0.05$, $^{**}p < 0.01$, $^{***}p < 0.001$, and $^{****}p < 0.0001$. Graphs were plotted in OriginPro 9 (OriginLab Corp, USA).

3. Results and discussion

Traditionally, 2D *in vitro* models cannot capture the complexity of the dynamic brain microenvironment. Therefore, 3D bioprinting offers an innovative platform to emulate the intricate cellular interactions within the NSC niche. NSCs cultured in a non-adherent condition proliferate and form clonal neurospheres that mimic the spatial arrangement and architecture of a neurogenic niche.[22,31] Here, we demonstrate that bioprinted NSCs-derived neurospheres from six-week-old C57BL/6 mice with 1 μM $Aβ_{1–42}$ oligomers could mimic the environmental conditions and cellular organization of neurogenic niche, establishing an innovative model to study SVZ-derived NSCs in AD.

3.1. Biomaterial production and characterization

Previous studies in the literature demonstrate the efficiency of ALG and GEL as a base for biomaterials[21,32–34] and bioprinting processes.[35,36] We tested several hydrogel compositions before selecting the one used in this study, including different concentrations of ALG-GEL, as well as adding agarose, Geltrex™, poly-L-lysine, and laminin (data not disclosed). The printability of the selected hydrogel composition was the most suitable for this study, promoting neurosphere encapsulation, survival, and growth, as well as retention of Aβ. Laminin, one of the main components of Geltrex™ and a potential component to facilitate cell spreading, is known to interact with Aβ[37–39], moreover, photocrosslinking with UV light could damage both cells and Aβ aggregates, consequently, we decided not to use them to produce our constructs.[40–42]

GEL, a collagen-derived protein, changes from gel to liquid state at 35–40°C, losing its ability to gel above such temperatures. It has attracted tremendous attention in bioprinting due to its high biocompatibility and hydrophilicity,[43] especially when mixed with other biomaterials to form double-network constructs with improved printability and cell functions.

In contrast, ALG, a biocompatible, biodegradable, and non-toxic polysaccharide, has better mechanical properties and represents the most commonly bioprinted material.[44] It is easily gelled when crosslinked with a divalent cation, e.g., Ca^{2+}, forming rigid hydrogels, ensuring long-term morphological stability and water retention. However, ALG alone has limited biological inertness, low cell attachment, adhesion properties, and biological activity.[45,46]

Since GEL solutions have desirable viscosity and tunable properties at temperatures lower than 25°C (depending on the polymer concentration and bloom value), blending GEL with ALG, a more viscous polymer, makes it possible to generate hydrogels with good flow and shape-retention

characteristics.[47,48] The presence of GEL facilitates rapid gelation of the construct during the bioprinting process at room temperature (compared to ALG-crosslinked with Ca^{2+} alone) and strengthens the ALG structure in a thermoresponsive manner, consequently improving the initial stability of the hydrogel.[36] Therefore, considering that the optimal polymeric concentration of a hydrogel should range from 10 to 20%,[49] our formulation consisted of 6% ALG + 4% GEL, leveraging the advantages of both polymers and displaying great promise for modeling the NSC environment (Figure S1, Supporting Information; Videos S1–S4, Supporting Information).[28,33]

Figures 1–3 present the characterization of both the hydrogel and the bioprinted construct. The polymeric blend was first printed without cells to determine the best design for printability and to measure wettability, surface roughness/porosity, degradation, and swelling rates. Furthermore, the mechanical and structural characteristics, as well as the electrical conductivity, were evaluated accordingly.

Code 2 (Figure 1A) was designed for the characterization assays. The wettability profile of the bioprinted hydrogel (crosslinked or not) is presented in Figure 1B, displaying snapshots and contact angle measurements every 2 min until complete absorption of a drop of water into the samples. The initial contact angle of the crosslinked hydrogel was 55.3 ± 0.2°, while that of the non-crosslinked hydrogel was 30.4 ± 0.4°. The crosslinked hydrogel fully absorbed the water droplet after 38 min, while the non-crosslinked hydrogel took less than 2 min, indicating that crosslinking is essential to harden the material while maintaining its hydrophilicity.

Hydrogel degradation was monitored for 28 days, with constructs immersed in dH_2O or DMEM/F12 at 37°C and 5% CO_2 (Figure 1E). In both conditions, the constructs maintained approximately 50% of their initial weight (49.6 ± 4.6% in DMEM/F12; 46.9 ± 4.2% in dH_2O) ($p < 0.001$ relative to their respective initial weight), suggesting that, despite the high degradability rate, constructs preserved their 3D structure for nearly a month. The sustained degradation over time might increase the construct's porosity and promote essential biological functions, as cells are more prone to migrate, proliferate, and differentiate when the surrounding network structure is less dense.[50]

Several factors may have influenced the degradability rate of the hydrogel, such as the concentration and duration of $CaCl_2$ crosslinking, the M_W of ALG, the concentration of both polymers, and the swelling rate[35,45,50–53]. Freeman and Kelly[51] reported that low-M_W ALG hydrogels (3.5%) had significant degradation over 21 days in culture, while high-M_W ALG hydrogels (3.5%) displayed little to no degradation. Additionally, Sonaye *et al.*[53] demonstrated that higher concentrations of ALG (8–12%) compared to GEL (6%), along with high crosslinking concentrations of $CaCl_2$ (300–500 mM), enhanced the swelling capacity and decreased the breakdown rate of hydrogels.

Considering the swelling profile (Figure 1F), when constructs were incubated in DMEM/F12 or dH_2O, the percentage of wet mass on day 2 was approximately 40% greater than the dry mass on day 0, demonstrating that constructs are easily tumefied by medium (or dH_2O) absorption. Over time, the swelling rate gradually decreased, as the structures degraded. Sonaye *et al.*[53] reported a similar phenomenon with their ALG-GEL hydrogels. Scaffolds with a greater ALG concentration swelled by 70%, peaking at day 4 to a saturation point, and started to disintegrate on day 8. As a result, their 3D model completely degraded within 14 days of incubation in DMEM. Kaliampakou and colleagues[50] also tested multiple blends of ALG-GEL hydrogels with varying $CaCl_2$ concentrations and crosslinking durations. They described that the best configuration (8% ALG+ 4% GEL; 248 mM $CaCl_2$; 15 min crosslinking) resulted in a hydrogel degradation time of ~20 days with a swelling ratio of 50%.

Unlike the constructs generated in the present study, none of the aforementioned materials was able to maintain their structure for the achieved benchmark duration of 28 days. Thus, the 6% ALG+ 4% GEL hydrogel produced constructs capable of retaining cell culture medium while also facilitating the diffusion of soluble components for supporting cellular growth within the core without entirely degrading the 3D structure in a short period.

The construct's morphology, analyzed by SEM, maintained a smooth and uniform surface for up to 14 days (Figure 1C). Polymeric homogeneity represents an important attribute of the hydrogel because heterogeneity in its structure can jeopardize cellular adhesion and survival due to the formation of polymeric clumps and cytotoxic aggregates.[54]

The size loss displayed in Figure 1D could be attributable to GEL thermal stability, as it can liquefy and release from the construct when incubated at 37°C.[52,55] Despite this, our hydrogel lasted longer than any ALG-GEL blend cited in this section, indicating that this composition delayed GEL release from the scaffolds by trapping it within the crosslinked ALG blocks.[55]

Rheological analysis was performed to investigate the fluidity and viscoelastic behavior of the hydrogel, as well as its viscosity under constant shear stress and strain (Figure 2). These assessments can provide key information about the printability of the hydrogel, the impact of forces

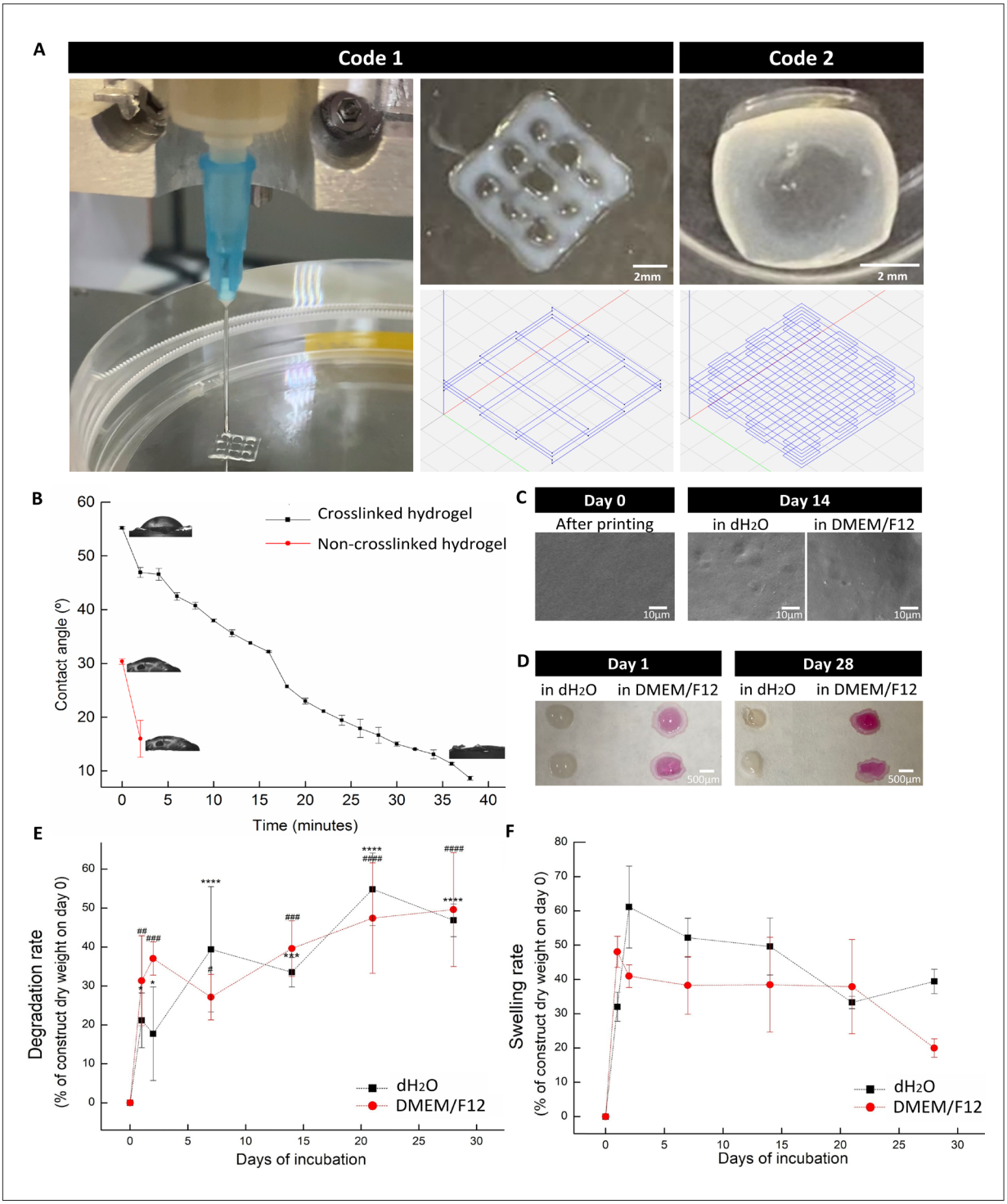

Figure 1. Characterization of the materials. (A) Codes 1 and 2 are designed by G-code and printed: macroscopic view of the bioprinting process, constructs, and G-code design. (B) Contact angle and wettability periodic scheme of crosslinked and non-crosslinked constructs (n = 3 per group). (C) SEM micrographs of the constructs immediately after printing and 14 days after immersion in dH_2O or DMEM/F12, respectively. (D) Macrographs of dried constructs after immersion in dH_2O or DMEM/F12 for 1 and 28 days, respectively. (E) Degradation rate of crosslinked constructs immersed in dH_2O or DMEM/F12 for up to 28 days (n = 4 per group, per period) ($^{*}p < 0.5$; $^{***}p < 0.001$; $^{****}p < 0.0001$; $^{\#\#}p < 0.1$; $^{\#\#\#}p < 0.001$; and $^{\#\#\#\#}p < 0.0001$, compared to the individual mass of the constructs after printing at day 0) (F) Swelling rate of crosslinked constructs immersed in dH_2O or DMEM/F12 for up to 28 days. Scale bars: 2µm (A); 10 µm (E); and 500 µm (F). Abbreviations: dH_2O: Distilled water; DMEM/F12: Dulbecco's modified eagle medium/nutrient mixture F-12; and SEM: scanning electron microscopy.

required for extrusion on its structure, and its ability to recover post-extrusion, maintaining the original shape of the 3D-bioprinted material.[56] Mechanical and rheological characterizations are also fundamental for understanding the influence of hydrogel network structures on the biological properties in the 3D-bioprinted model.[56,57] Nevertheless, according to a systematic review,[58] only 12.1% out of the 118 analyzed papers performed rheological characterization or detailed the viscosity of the hydrogels developed for 3D bioprinting.

A continuous shear rate sweep was performed to simulate the shear stress that the bioink undergoes in a 3D extrusion bioprinting process as it passes through the nozzle. The flow behavior and viscosity of the hydrogel obtained in this analysis are plotted as rheograms (Figure 2A and B). The ALG-GEL hydrogel behaved as a non-Newtonian fluid with pseudoplastic behavior and thixotropy. A pseudoplastic fluid (also called a shear-thinning material) exhibits a decrease in viscosity when the shear rate increases[59,60] which is crucial for 3D printing since the viscosity of the hydrogel decreases during extrusion. This viscosity reduction avoids excessive extrusion pressures that can negatively affect cell viability during the printing process.[61] The hydrogel also displayed minimal thixotropy with a narrow hysteresis loop, indicating that after extrusion, the hydrogel will recover its original structure at rest rather than continuing to flow as a fluid.[62]

The presence of yield stress, as depicted in Figure 2B, is another important component. Hydrogels composed of materials with solid-like properties typically have yield stress, making them promising candidates for 3D bioprinting.[63] The hydrogel behaves like a solid when it is at rest, e.g., when the bioink containing the cell suspension is in the syringe. It will not flow unless it is subjected to a specific stress, such as pressing the syringe plunger, that surpasses the yield stress. This behavior enables the hydrogel to be extruded in a controlled manner and rapidly recover its solid-like characteristics after the applied force is removed, right before crosslinking.[56,64]

Although the hydrogel demonstrated flow behavior and a viscosity profile that are critical for 3D bioprinting, the oscillatory studies yielded unexpected results. Figure 2D and E illustrates that the hydrogel behaves as a viscous material ($G'' > G'$) across a wide range of frequencies and strains. In both oscillatory sweeps, the loss modulus (G'') was greater than the storage modulus (G'), indicating that the hydrogel has a fluid structure and may be classified as a viscoelastic liquid.[65] Figure 2E also depicts the phase angle or loss tangent ($\tan \delta = G''/G'$), which confirms these results, where $\tan \delta < 1$ indicates a solid-like state of the hydrogel, and $\tan \delta > 1$ indicates a liquid-like state.[65,66] At low oscillatory strain, the ALG-GEL hydrogel reported $\tan \delta > 3$, which reduced with increasing strain stress but remained greater than 1. As the $\tan \delta$ value approached 1 (upon 60% strain), the hydrogel complex viscosity increased, indicating a potential transition from a liquid-like to a solid-like state (where G' dominates G'' and $\tan \delta < 1$) (Figure 2F).

To assess the mechanical strength of the hydrogel composition before and after crosslinking with 2% $CaCl_2$ solution (construct), the storage modulus and phase angle of the hydrogel and the construct were determined at 1 Hz frequency and 1% strain, respectively. Figure 2G and H indicates that constructs had G' values nearly tenfold higher than the hydrogel (10 kPa), suggesting that the presence of an ionic crosslinker promoted the formation of a harder/stiffer structure with elastic character ($\tan \delta < 1$), most likely due to interactions between Ca^{2+} ions and ALG chains.[67] Although the presence of GEL may enhance the biological and physicochemical properties of ALG due to the tripeptide Arg-Gly-Asp (RGD) sequence that facilitates cell attachment,[68,69] the uncrosslinked hydrogel did not present viscoelastic solid-gel behavior ($G' < 10$ Pa; $\tan \delta > 1$), possibly due to weak internal chemical bonds between the two biopolymers.

The hydrogel developed in the present study exhibited viscoelastic characteristics ($G' < G''$ $\tan \delta > 1$) that differ from other ALG-GEL hydrogels reported in the literature. Several studies characterize these hydrogels as having gel-like behavior and elastic mechanical characteristics.[70–73] However, when comparing these results, various aspects must be considered, the most important of which is the GEL: ALG ratio. Blending GEL with ALG boosts the hydrogel's viscosity and elastic behavior, as the ideal mechanical characteristics of ALG hydrogels are heavily influenced by the polymer's molecular weight and concentration, as well as the ionic crosslinker used.[72,74,75] Furthermore, some researchers noted that cooling the hydrogels before printing could result in overall gel properties that are more suitable for higher print resolution due to GEL's thermoresponsive qualities.[76]

Chung *et al.*[76] described that GEL hydrogels with low ALG concentration (2%) behave like fluids ($G'' > G'$) at room temperature (25°C) or higher, consistent with our findings. Maihemuti *et al.*[77] demonstrated that when fish GEL is blended with ALG, the printability is determined by the concentration of ALG rather than the GEL itself, the finding of which supports our results. In their study, hydrogels were only printable and stable when they included 6% ALG, which kept the viscosity within a printable range that was neither too high to extrude nor too low to maintain the shape.

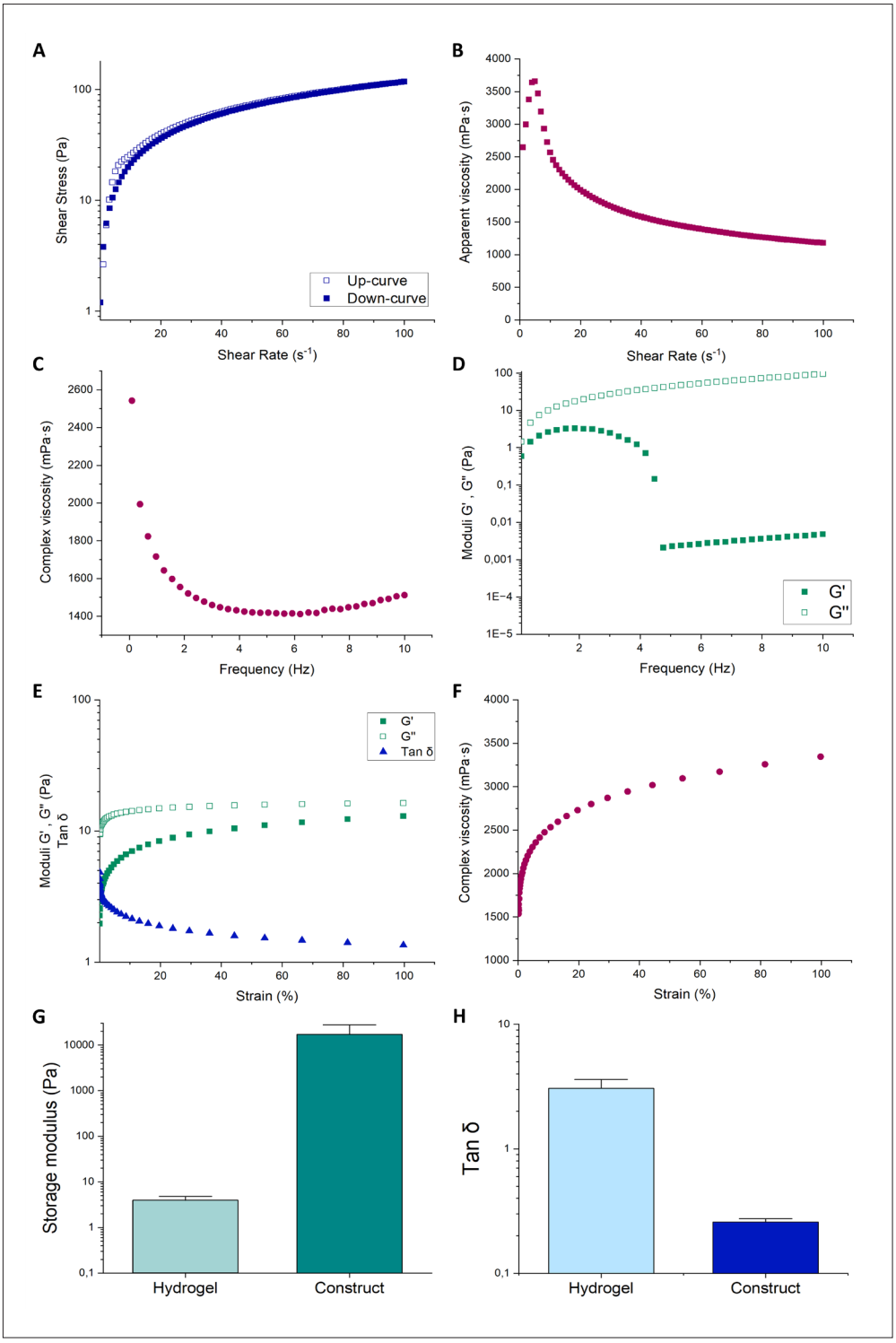

Figure 2. Rheological characterization of the materials. (A) Flow curves of the hydrogel display minimal thixotropy. Filled symbols indicate an upward curve; empty symbols indicate a downward curve. (B) Viscosity as a function of increasing shear rate reveals the shear-thinning behavior of the hydrogel. (C) Complex viscosity vs. frequency. (D and E) Storage modulus (G'; filled symbols) and loss modulus (G"; empty symbols) obtained from a frequency sweep test (D) and an amplitude sweep test (E) demonstrated the hydrogel's viscous behavior. (E) Oscillatory analysis also revealed that, upon increasing strain stress, the loss factor (tan δ) declined but remained greater than one (tan $\delta > 1$), emphasizing how the hydrogel behaves as a viscous liquid. (F) On the other hand, the complex viscosity rose. (G and H) The storage modulus (G) and loss factor (H) of both hydrogel and construct at frequency = 1 Hz and strain = 1%. All rheological measurements were performed at 25°C. Data are plotted as the mean values from three replicates.

Given that GEL liquefies at 37°C, a hydrogel containing more GEL than ALG would gradually deteriorate during incubation and disintegrate within a few days, shortening the time for cell culture. Therefore, we utilized a hydrogel with greater ALG content to prevent such drawbacks. Although our hydrogel exhibited viscoelastic-liquid behavior throughout our oscillatory rheological measurements, it could still be printed and maintain its original shape post-extrusion, indicating a promising profile for use as a bioink for cellular culture in a 3D environment.

The chemical structure composition of the bioprinted hydrogel (crosslinked or not), the crosslink agent $CaCl_2$, and the polymeric components of the hydrogel, ALG, and GEL, were analyzed by ATR-FTIR spectroscopy (Figure 3A). In the ALG spectrum, the transmission bands at 1600 and 1410 cm^{-1} represent the asymmetric and symmetric vibrations of COO^-, respectively, while the bands at 1090 and 1030 cm^{-1} are attributed to C-O and C-O-C bonds.[78,79] In GEL, the bands observed at 1630, 1543, and 1238 cm^{-1} are attributed to the amide I, II, and III vibration peaks, respectively. The crosslinked hydrogel exhibited all the bands mentioned above. However, the amide I band of GEL is obscured by the strong absorption band at 1600 cm^{-1} of ALG, attributed to the asymmetric stretching of the COO^- vibration, and shifted to a discretely lower wavelength, suggesting that there was an interaction between the positive charges of the amino group of GEL and the negative charges of the terminal COO^- groups of ALG. Additionally, as there was more ALG than GEL in the hydrogel, the characteristic bands of GEL diffused with reducing chain order. Notably, crosslinking with $CaCl_2$ did not modify the main structures of the hydrogel.

As our primary goal is to develop a 3D model for AD, we investigated whether the presence of Aβ in the hydrogel composition would affect its structure. In Figure 3B and C, we present the characterization of the Aβ structure alone and the structure after incorporation into the hydrogel with neurospheres as oligomeric/fibrillary structures. The main amide I band (1700–1600 cm^{-1}) of the Aβ peptide backbone is correlated with oligomer size, where larger oligomers are associated with lower wavenumbers.[80] The amide I band of Aβ was at 1625 cm^{-1}, representing Aβ oligomeric arrangement.[81–83] This is an important feature once monomeric Aβ is found in healthy brains. However, oligomers and fibrils are toxic and are the components of amyloid plaques, one of the AD hallmarks.[12,84,85] The amyloid or senile plaques are responsible for increasing oxidative stress, contributing to neuronal dysfunction, disruption of synaptic function, compromising neuroplasticity, decreasing memory formation, and inducing neuroinflammation.

The electrical conductivity of the hydrogel was also evaluated. This parameter is essential for understanding the physicochemical relationship between biological and artificial systems,[86] mimicking physiological electrical processes. *In vivo*, electrical conductivity facilitates neuronal communication[87,88] and directs NSC maturation into functional neuronal networks.[89] Even without externally applied electric fields, conductive hydrogels promote neurite outgrowth and NSC differentiation, efficiently contributing to the native CNS support for neural cells.[90] At room temperature, the hydrogel we produced has an electrical conductivity of 27.46 mS/cm. Conductivity measurements for native CNS tissues (matrix and cells) ranged from 2 to 7 mS/cm,[89] indicating a closer conductivity of the bioink to the brain tissue. High-conductive biomaterials for neural applications could reach up to 17 S/cm[91] to specifically electro-stimulate NSCs and up to 7500 S/cm for further biomedical applications.[92]

3.2. Aβ oligomers incorporated into the bioink induce a decrease in cell viability and an increase in oxidative stress

Neurospheres are free-floating populations derived from neural stem and progenitor cells isolated from the neurogenic niches (dentate gyrus of the hippocampus or the SVZ).[93] In the constructs we produced, Aβ was incorporated into the bioink rather than inside the neurospheres, aiming at mimicking senile plaques distributed within the neurogenic niches and in the brain parenchyma of AD patients as extracellular deposits. The neurosphere structure was maintained in the bioink, and Aβ oligomers were retained within the hydrogel, simulating one of the pathological features of AD, i.e., the deposition and accumulation of Aβ in the extracellular microenvironment.

Simpson *et al.*[94] demonstrated that Aβ aggregates more readily in a 3D environment of collagen hydrogel than in 2D, suggesting that a 3D environment may increase Aβ-Aβ interactions, accelerating aggregation and shifting Aβ organization from oligomers to fibril. According to the authors, Aβ aggregation kinetics is fundamentally different in 3D structures compared to a 2D environment.

A critical issue in modeling the neural tissue is optimizing cell density to ensure that they will be properly preserved within the construct and viable after printing.[95] Moreover, to achieve optimal printability and provide a proper 3D matrix, cells must be compatible with the hydrogel to proliferate and/or differentiate within it. It is recognized that cytoviability can be reduced by extrusion-based bioprinting due to the high shear force exerted on the cells by the printing nozzles.[96] Using code 1 (Table 2; Figure 1A), we demonstrate that the total area of the neurospheres

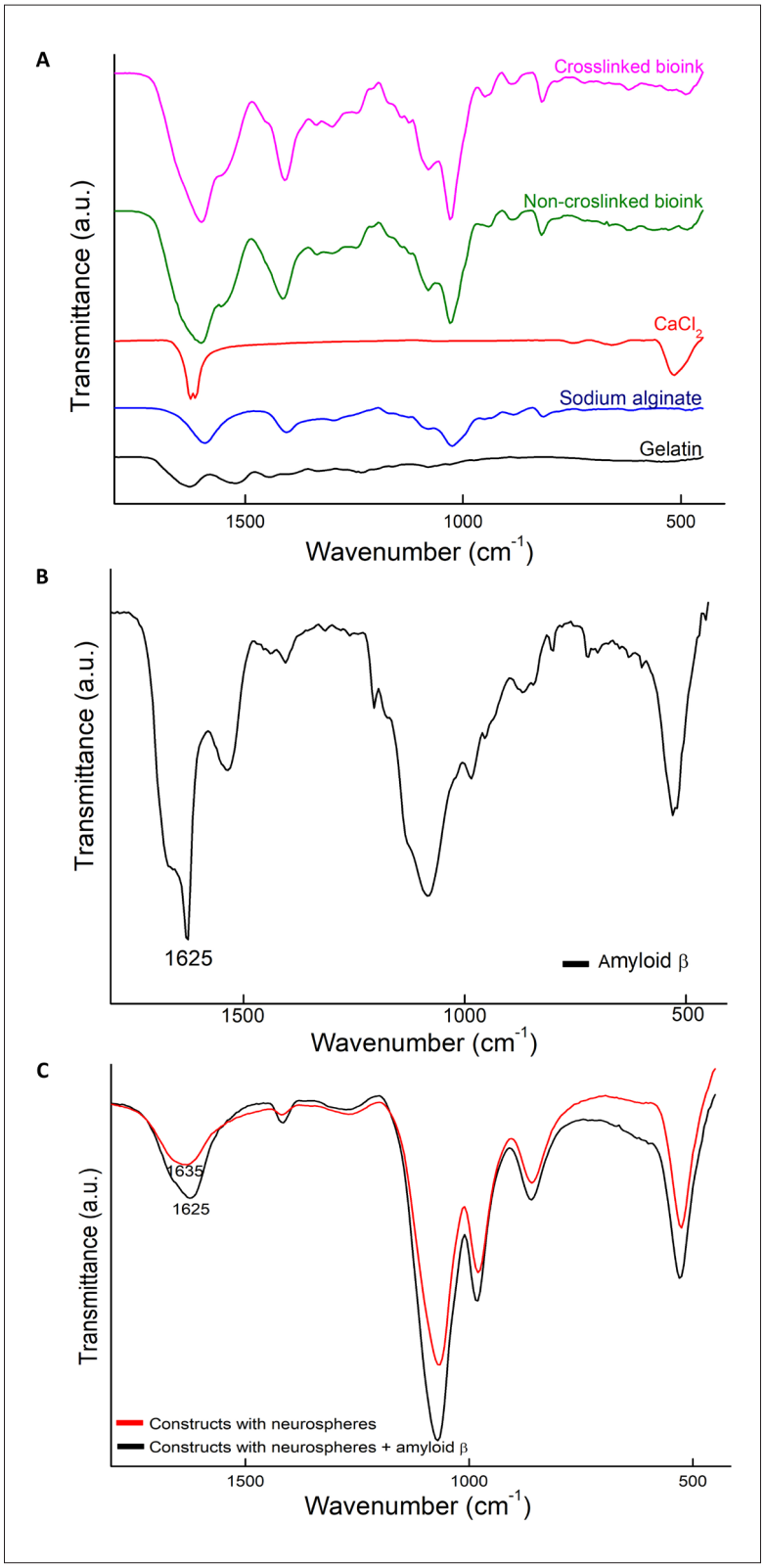

Figure 3. Attenuated total reflectance-Fourier transform infrared (ATR-FTIR) spectra of (A) constructs crosslinked (magenta) and non-crosslinked (green) with $CaCl_2$, $CaCl_2$ alone (red), and hydrogel components sodium alginate (ALG; blue) and gelatin (GEL; black); (B) oligomerized amyloid β (Aβ); and (C) constructs with neurospheres with and without Aβ oligomers.

bioprinted in the absence of Aβ oligomers increased up to eight days after bioprinting ($p < 0.0001$; day 8 vs. day 0 [immediately after bioprinting]) (Figure 4A and B). This growth in the neurosphere area corresponded to increased cell proliferation (379.8 ± 7.7%) on day 8 compared to day 0 ($p < 0.0001$; immediately after bioprinting) (Figure 4C).

Although a recent study has emphasized the great potential of neurospheres from transgenic animals for evaluating familial AD,[97] in this study, we prioritized the Aβ extracellular oligomers in the 3D model in the NSC environment. This decision was based on the fact that over 95% of AD cases are sporadic instead of familial,[98,99] and *in vitro* models for this form of AD are scarce.

The area of the neurospheres bioprinted in the hydrogel containing Aβ oligomers did not increase over time (Figure 4B). Although there were smaller neurospheres on day 8 compared to day 0 (Figure 4A), the average size did not statistically change. A pronounced negative effect on cell proliferation/viability was observed in neurospheres bioprinted in the hydrogel containing Aβ oligomers (52.7 ± 16.5% for day 3; 8.02 ± 3.1% for day 8; $p < 0.0001$, compared with constructs bioprinted in the hydrogel

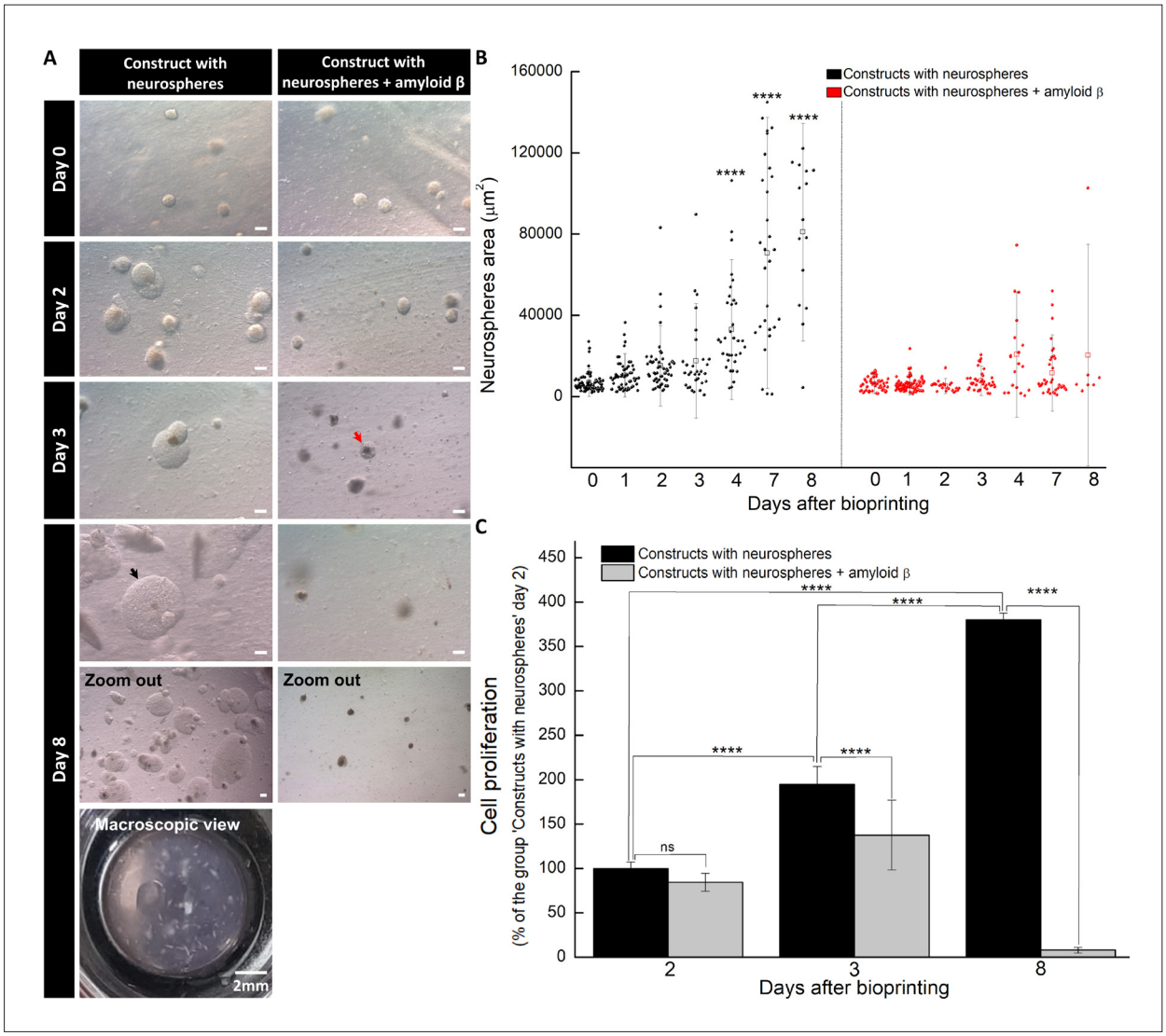

Figure 4. Amyloid β (Aβ) oligomers impact neurosphere area and proliferation in the 3D constructs. (A) Light microscope micrographs of constructs with neurospheres from the subventricular zone (SVZ) of six-week-old C57bl/6 mice, bioprinted with or without 1 μM Aβ oligomers. The black arrow indicates the well-delimited and spheroidal surface of the neurosphere, even eight days after bioprinting. The red arrow demonstrates the necrotic core and small neurospheres three days after bioprinting. Scale bars: 100 μm. (B) Area of neurospheres in constructs with and without Aβ oligomers ($^{****}p < 0.0001$, compared with neurospheres area from day 0). (C) Cell proliferation in constructs with and without Aβ oligomers ($^{****}p < 0.0001$; and ns: non-significant).

without Aβ oligomers and cultured for the same periods) (Figure 4C). These results corroborate a recent study by Esteve *et al.*, which demonstrated that an Aβ-induced increase in reactive oxygen species (ROS) levels led to DNA damage and subsequently induced cell cycle arrest with an increase in cadherin-1 (Cdh1) and a decrease in cyclin B1 and cyclin-dependent kinase 5 (Cdk5)/p35 expression.[100] Moreover, it was demonstrated that exposing neurospheres from prenatal rat cerebral cortical regions to Aβ decreases cell viability and induces degeneration of neurites and apoptosis.[101] Bernabeu-Zornoza *et al.*[102] reported that 1 μM $Aβ_{40}$, the same concentration we used, induced cell death in the human NSC cell line hNS1.

As the neurosphere area and proliferative assay demonstrated small and lowly proliferative cells on day 8 in constructs with Aβ oligomers, the following assays were performed 2–3 days after bioprinting. On day 2 after bioprinting, the live/dead assay demonstrated that cells in the neurospheres within the constructs are viable, and phalloidin staining revealed that the neurospheres have a well-structured spheroid shape and a complex and dense cytoskeleton arrangement (Figure 5A).

Oxidative stress is one of the main pathological events in AD, causing damage to biomolecules, such as neuronal membrane proteins and lipids, affecting their integrity, contributing to neuronal death, and directly impairing NSC proliferation and survival.[103] Aβ oligomers may trigger the generation of ROS, which impairs neurogenesis. There is a vicious cycle whereby Aβ oligomers induce increased ROS levels and oxidative stress, consequently raising Aβ production and leading to AD.[104,105] ROS can cause DNA damage, leading to genomic instability in NSCs. As displayed in Figure 5B and C, oxidative stress significantly increased in constructs containing Aβ oligomers in the bioink as early as 2 days after bioprinting. The same increase in oxidative stress in NSCs exposed to Aβ oligomers was observed by Chiang *et al.*[105], and the oxidative stress also increased the expression of pro-inflammatory cytokines TNF-α and IL-1β. Consequently, the ability of NSCs to proliferate and generate functional neurons may be compromised, contributing to cognitive decline.

Interestingly, oxidative stress can be transiently generated by neurogenesis,[106,107] which could explain the increased ROS production and enhanced neurogenesis in constructs containing Aβ oligomers (Figures 5 and 6). Some evidence indicates that NSCs are well-adapted to protect their host environment from oxidative stress,[108] leading to a synergistic effect between ROS and neurogenesis when the brain is trying to protect or compensate for neuronal loss.

3.3. Exposing cells to Aβ oligomers induces morphological changes and neurogenesis

Three days after bioprinting, an evident morphological change was observed on the surface of constructs with and without Aβ oligomers (Figure 5D). SEM images revealed that constructs without neurotoxic aggregates presented a homogeneous and smooth surface, whereas adding 1 μM Aβ oligomers made the constructs' surface rougher.

A reduction of NSCs (Figure 6; $Nestin^+$ cells, stained in red) and an increase of mature neurons (Figure 6; $MAP\text{-}2^+$ cells, stained in green) within the neurospheres in constructs with Aβ oligomers is presented in Figure 6C ($p < 0.0001$, compared with constructs without Aβ oligomers). The 3D reconstitution of a stained neurosphere displays more mature neurons in the constructs with Aβ oligomers than NSCs, compared to constructs without Aβ oligomers (Figure 6A and B). $Nestin^+$ cells represent 42.4 ± 9.9% of the total stained area of neurospheres in constructs without Aβ oligomers, while in the presence of the aggregates, the percentage decreases to 26.8 ± 9.6% (Figure 6C). Conversely, mature neurons correspond to 14.8 ± 8.6% of the stained area of constructs without Aβ aggregates, while in constructs with Aβ oligomers, mature neurons represent 29.6 ± 9.3% (Figure 6C).

It is important to emphasize that NSCs in the neurospheres were not stimulated to differentiate by adding a differentiation medium, which can also modulate neurogenesis and neurosphere morphology (Figures S2 and S3, Supporting Information). Neurogenesis observed in Figure 6 is mainly induced by the 3D bioink environment or the presence of Aβ. *In vivo*, as AD progresses, the neurotoxicity of Aβ increases, and when coupled with other elements, such as glucose uptake imbalance[9] and dysregulated insulin signaling, adult neurogenesis is increasingly inhibited. Notably, bioprinting Aβ oligomers instead of incorporating them into the neurospheres allowed our model to mimic the extracellular deposit of Aβ aggregates that surround the neurogenic niches in the brain of patients with AD.

Neurospheres used in this study are derived from six-week-old mice, representing adult but not aged conditions. In adults, Aβ oligomers distributed in the 3D environment may stimulate neuronal differentiation as a mechanism to overcome future impairment in AD progression. By increasing oxidative stress, autophagy is induced to meet high energy demands.[109,110] Consequently, neurogenesis is increased as a response to NSC impairment caused by the disease. Another hypothesis is that in earlier stages of AD, Aβ oligomers can activate a compensatory mechanism to replace lost or damaged cells by increasing the differentiation of neuronal progenitors into new neurons. However, as

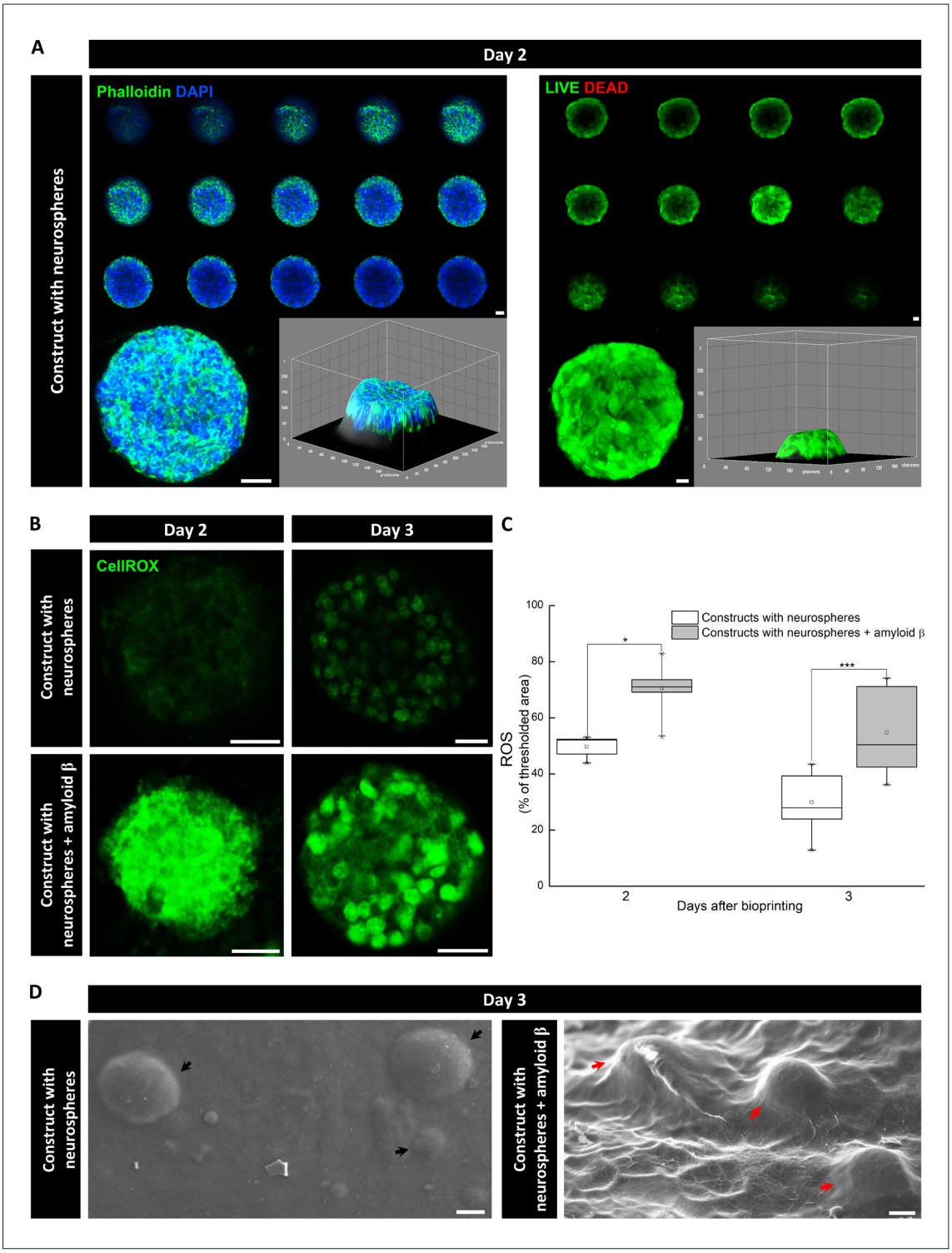

Figure 5. Amyloid β (Aβ) oligomers modify the morphological aspects and induce oxidative stress in the 3D constructs. (A) Montage of stained Z-projection, followed by 3D-plot reconstitution of one representative neurosphere stained with phalloidin/DAPI and LIVE/DEAD kit assay, respectively, two days after bioprinting. (B) Oxidative stress assay in the neurospheres, using the CellROX reagent, on days 2 and 3 after bioprinting. (C) Quantification of reactive oxygen species (ROS) in the neurospheres of the constructs, on days 2 and 3 after bioprinting ($^{*}p < 0.5$; $^{***}p < 0.001$). (D) Scanning electron microscopy (SEM) micrographs of the surface morphology of constructs without and with Aβ oligomers three days after printing. Black arrows indicate neurospheres immersed in a smooth construct surface. Red arrows indicate neurospheres within a rough construct under Aβ oligomers exposure. Scale bars: 20 μm.

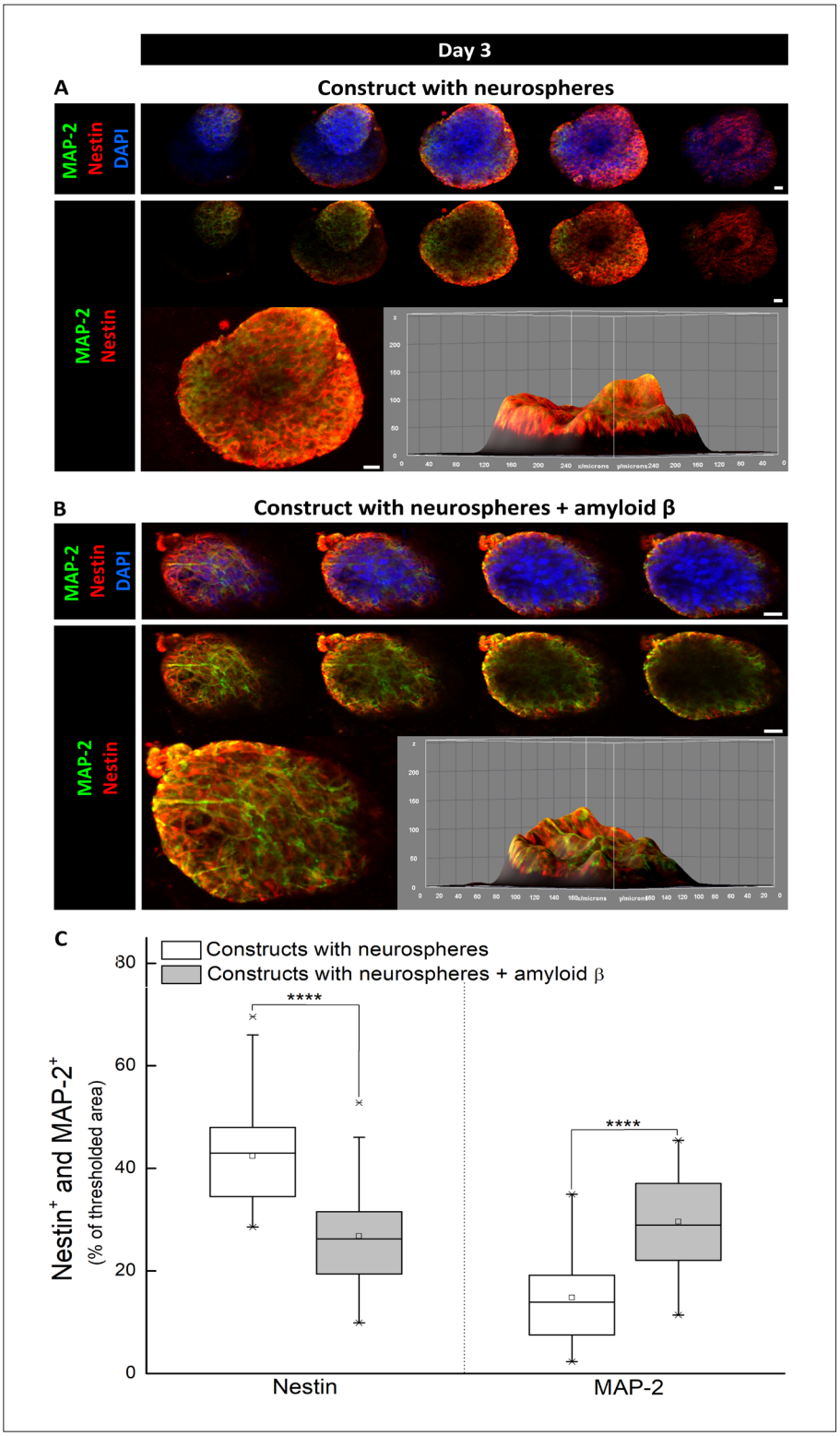

Figure 6. Amyloid β (Aβ) oligomers in 3D constructs induce neural stem cell (NSC) differentiation three days after bioprinting. (A) Construct with neurospheres. (B) Construct with neurospheres + Aβ oligomers. The micrographs indicate a sequence of neurosphere staining, where blue: DAPI (nuclei), green: MAP-2$^+$ (mature neurons), and red: Nestin$^+$ (NSCs), followed by a Z-projection of MAP-2$^+$ and Nestin$^+$ cells. Scale bars: 20 μm. The 3D plots reconstitute the surface of the constructs, where stained cell distribution can be observed from a 3D perspective. (C) Quantification of Nestin$^+$ and MAP-2$^+$ cells in constructs with and without Aβ oligomers ($^{****}p < 0.0001$; × indicates maximum or minimum values; and ◘ indicates the mean).

time passes and senile plaques are formed, the imbalance creates an increasingly neurotoxic environment.[111]

Studies in the literature corroborated the effects of Aβs in promoting gliogenesis[112] or neurogenesis[102] in human NSCs and NSCs from rat hippocampus,[111] impairing NSC proliferation and stimulating microglial proliferation.[8–10,12,113] Another *in vitro* study demonstrated that exosomes secreted from NSCs, but not mature neurons, may confer resistance to the dysfunctional impact of Aβ oligomers,[114] indicating the possible neuroprotective potential of NSCs.[115]

Once incorporated into the 3D microenvironment of our bioprinted neurospheres, Aβ oligomers and other secreted factors may be effectively retained within the matrix environment, mimicking the NSCs environment. Our findings are in accordance with previous reports which indicate that Aβ oligomers promote neurogenesis and neuronal differentiation[85,111] even in the hippocampus of humans with AD.[116] Sotthibundhu *et al.*[12] also observed that Aβ stimulates adult neurogenesis in neurospheres derived from NSCs extracted from the SVZ of two-month-old mice.

Although it has been demonstrated that higher levels of Aβ monomers, oligomers, and fibrils in the brain microenvironment of individuals with amyloidosis-β-induced oxidative stress have a negative effect on endogenous neurogenesis,[117] AD is a progressive and dynamic disease. It is plausible that an increase in neuronal differentiation is followed by an overall decline as Aβ aggregates and loses its neurogenic-inducer functions.[109] Consequently, neurogenesis is differentially regulated throughout the disease, possibly contributing to its progression.

While most AD studies focus on hippocampal neurogenesis in older mice (2–10 months) with AD genotype and demonstrate impaired neurogenesis,[3] it is essential to explore diverse brain regions. In this regard, engineering adult NSCs niche is a valuable tool.[118] Here, we fabricated a 3D model of the adult SVZ-NSCs environment in AD. Although cell viability is impaired and oxidative stress is raised, NSCs differentiate more into neurons when exposed to Aβ oligomers, and we presume this could be a compensatory mechanism of the neurogenic niche, which can be further investigated and tested using the bioprinted model we developed.

4. Conclusion

The constructs we fabricated and characterized successfully reproduced the NSC environment of AD with Aβ oligomer modulation, subsequently decreasing cell viability, increasing oxidative stress, and inducing neuronal differentiation of NSCs. We explored the application of 3D bioprinting to engineer a physiologically relevant model that mimics the cellular composition and dynamic interactions observed in the adult neurogenic niche, highlighting the different pathways of AD.

Acknowledgments

The authors would like to thank Clara Pompeu Ferreira (Universidade Federal de São Paulo) for providing the neurospheres, and MSc. Henrique Correa and Prof. Dr. Beatriz O. Monteiro (Universidade Federal de São Paulo) for providing Aβ oligomers. We are grateful to the technicians, MSc. Priscila M. S. C. M. Leite and Dr. Angela A. M. Vieira (Instituto de Pesquisa e Desenvolvimento, IP&D, Universidade do Vale do Paraíba), for their assistance with SEM and FTIR. We are grateful to Prof. Dr. Fabiana Perrechil Bonsanto (Laboratory of Biotechnology and Natural Products, BioNat, Universidade Federal de São Paulo), for providing the rheometer for our rheological analysis. We thank the technicians, Elizabeth N. Kanashiro and Carolina Z. Romera, for their assistance with the confocal microscope (Universidade Federal de São Paulo).

Funding

This study was supported by grants from (i) the São Paulo Research Foundation (FAPESP): Grants 2022/08664-4 (GRS), 2023/08040-3 (NDF), and 2018/12605-8 (MAP); and (ii) the Brazilian National Council for Scientific and Technological Development (CNPq): 406258/2022-8, INCT Model 3D, and 152384/2024-3 (GRS).

Conflict of interest

The authors declare that they have no conflicts of interest. The research was conducted without any commercial or financial relationship.

Author contribution

Conceptualization: Marimelia Aparecida Porcionatto, Geisa Rodrigues Salles
Formal analysis: Geisa Rodrigues Salles
Investigation: All authors
Methodology: Geisa Rodrigues Salles, Natalia Dall'Agnol Ferreira, Paula Scanavez Ferreira
Writing – original draft: All authors
Writing – review & editing: All authors

Ethics approval and consent to participate

The Ethics Committee on the Use of Animals from the Universidade Federal de São Paulo (CEUA/UNIFESP;

Authorization number 2428100423) approved all experimental procedures in this study.

Consent for publication

Not applicable.

Availability of data

Data are available from the corresponding authors upon reasonable request.

References

1. Moreno-Jiménez EP, Flor-García M, Terreros-Roncal J, et al. Adult hippocampal neurogenesis is abundant in neurologically healthy subjects and drops sharply in patients with Alzheimer's disease. *Nat Med*. 2019;25(4):554-560. doi: 10.1038/s41591-019-0375-9
2. Selkoe DJ. Alzheimer's disease: genes, proteins, and therapy. *J Physiol Rev*. 2001;81(2):741-766. doi: 10.1152/physrev.2001.81.2.741
3. Li Puma DD, Piacentini R, Grassi C. Does impairment of adult neurogenesis contribute to pathophysiology of Alzheimer's disease? A still open question. *J Front Mol Neurosci*. 2021;13:578211. doi: 10.3389/fnmol.2020.578211
4. Kim HS, Shin SM, Kim S, Nam Y, Yoo A, Moon M. Relationship between adult subventricular neurogenesis and Alzheimer's disease: pathologic roles and therapeutic implications. *Front Aging Neurosci*. 2022;14:1002281. doi: 10.3389/fnagi.2022.1002281
5. Selkoe DJ. Alzheimer's disease. *Cold Spring Harb Perspect Biol*. 2011;3:a004457. doi: 10.1101/cshperspect.a004457
6. Culig L, Chu X, Bohr VA. Neurogenesis in aging and age-related neurodegenerative diseases. *Ageing Res Rev*. 2022;78:101636. doi: 10.1016/j.arr.2022.101636
7. Scopa C, Marrocco F, Latina V, et al. Impaired adult neurogenesis is an early event in Alzheimer's disease neurodegeneration, mediated by intracellular Aβ oligomers. *Cell Death Differ*. 2020;27(3):934-948. doi: 10.1038/s41418-019-0409-3
8. Salles GN, Calió ML, Afewerki S, et al. Prolonged drug-releasing fibers attenuate Alzheimer's disease-like pathogenesis. *ACS Appl Mater Interfaces*. 2018;10(43):36693-36702. doi: 10.1021/acsami.8b12649
9. Salles GN, Calió ML, Hölscher C, Pacheco-Soares C, Porcionatto M, Lobo AO. Neuroprotective and restorative properties of the GLP-1/GIP dual agonist DA-JC1 compared with a GLP-1 single agonist in Alzheimer's disease. *Neuropharmacology*. 2020;162:107813. doi: 10.1016/j.neuropharm.2019.107813
10. Calió ML, Mosini AC, Marinho DS, et al. Leptin enhances adult neurogenesis and reduces pathological features in a transgenic mouse model of Alzheimer's disease. *Neurobiol. Dis*. 2021;148:105219. doi: 10.1016/j.nbd.2020.105219
11. Diaz Brinton R, Ming Wang J. Therapeutic potential of neurogenesis for prevention and recovery from Alzheimer's disease: allopregnanolone as a proof of concept neurogenic agent. *Curr Alzheimer Res*. 2006;3(3):185-190. doi: 10.2174/156720506777632817
12. Sotthibundhu A, Li Q-X, Thangnipon W, Coulson EJ. Aβ1–42 stimulates adult SVZ neurogenesis through the p75 neurotrophin receptor. *Neurobiol Aging*. 2009;30(12):1975-1985. doi: 10.1016/j.neurobiolaging.2008.02.004
13. Bernabeu-Zornoza A, Coronel R, Palmer C, Monteagudo M, Zambrano A, Liste I. Physiological and pathological effects of amyloid-β species in neural stem cell biology. *Neural Regen Res*. 2019;14(12):2035-2042. doi: 10.4103/1673-5374.262571
14. Walus K, Beyer S, Willerth SM. Three-dimensional bioprinting healthy and diseased models of the brain tissue using stem cells. *Curr Opin Biomed Eng*. 2020; 14:25-33. doi: 10.1016/j.cobme.2020.03.002
15. de Melo BAG, Jodat YA, Cruz EM, Benincasa JC, Shin SR, Porcionatto MA. Strategies to use fibrinogen as bioink for 3D bioprinting fibrin-based soft and hard tissues. *Acta Biomater*. 2020;117:60-76. doi: 10.1016/j.actbio.2020.09.024
16. de Melo BAG, Benincasa JC, Cruz EM, Maricato JT, Porcionatto MA. 3D culture models to study SARS-CoV-2 infectivity and antiviral candidates: From spheroids to bioprinting. *Biomed J*. 2021;44(1):31-42. doi: 10.1016/j.bj.2020.11.009
17. Cruz EM, Machado LS, Zamproni LN, et al. A gelatin methacrylate-based hydrogel as a potential bioink for 3D bioprinting and neuronal differentiation. *Pharmaceutics*. 2023;15(2):627. doi: 10.3390/pharmaceutics15020627
18. Knowlton S, Anand S, Shah T, Tasoglu S. Bioprinting for neural tissue engineering. *Trends Neurosci*. 2018; 41(1):31-46. doi: 10.1016/j.tins.2017.11.001
19. Cadena M, Ning L, King A, et al. 3D bioprinting of neural tissues. *Adv Healthc Mater*. 2021;10(15):2001600. doi: 10.1002/adhm.202001600
20. Parra-Cantu C, Li W, Quiñones-Hinojosa A, Zhang YS. 3D bioprinting of Glioblastoma model. *J 3D Print Med*. 2020;4(2):113-125. doi: 10.2217/3dp-2019-0027
21. Gao T, Gillispie GJ, Copus JS, et al. Optimization of gelatin–alginate composite bioink printability using rheological

parameters: A systematic approach. *Biofabrication*. 2018;10(3):034106.
doi: 10.1088/1758-5090/aacdc7

22. Ioannidis K, Angelopoulos I, Gakis G, et al. 3D reconstitution of the neural stem cell niche: connecting the dots. *Front Bioeng Biotechnol*. 2021;9:705470.
doi: 10.3389/fbioe.2021.705470

23. Centeno EGZ, Cimarosti H, Bithell A. 2D versus 3D human induced pluripotent stem cell-derived cultures for neurodegenerative disease modelling. *Mol Neurodegener*. 2018;13:1-15.
doi: 10.1186/s13024-018-0258-4

24. Ioannidis K, Danalatos RI, Champeris Tsaniras S, et al. A custom ultra-low-cost 3D bioprinter supports cell growth and differentiation. *Front Bioeng Biotechnol*. 2020;8:580889.
doi: 10.3389/fbioe.2020.580889

25. Benwood C, Walters-Shumka J, Scheck K, Willerth SM. 3D bioprinting patient-derived induced pluripotent stem cell models of Alzheimer's disease using a smart bioink. *Bioelectron Med*. 2023;9(1):10.
doi: 10.1186/s42234-023-00112-7

26. Bovi dos Santos G, de Lima-Vasconcellos TH, Móvio MI, Birbrair A, Del Debbio CB, Kihara AH. New perspectives in stem cell transplantation and associated therapies to treat retinal diseases: from gene editing to 3D bioprinting. *Stem Cell Rev Rep*. 2024;20(3):722-737.
doi: 10.1007/s12015-024-10689-4

27. Romariz SAA, Sanabria V, da Silva KR, et al. High concentrations of cannabidiol induce neurotoxicity in neurosphere culture system. *Neurotox Res*. 2024; 42(1):14.
doi: 10.1007/s12640-024-00692-5

28. Fantini V, Bordoni M, Scocozza F, et al. Bioink composition and printing parameters for 3D modeling neural tissue. *Cells*. 2019;8(8):830.
doi: 10.3390/cells8080830

29. Zhou X, Cui H, Nowicki M, et al. Three-dimensional-bioprinted dopamine-based matrix for promoting neural regeneration. *ACS Appl Mater Interfaces*. 2018;10(10):8993-9001.
doi: 10.1021/acsami.7b18197

30. Joung D, Truong V, Neitzke CC, et al. 3D printed stem-cell derived neural progenitors generate spinal cord scaffolds. *Adv Funct Mater*. 2018;28(39):1801850.
doi: 10.1002/adfm.201801850

31. Suslov ON, Kukekov VG, Ignatova TN, Steindler DA. Neural stem cell heterogeneity demonstrated by molecular phenotyping of clonal neurospheres. *Proc Natl Acad Sci USA*. 2002;99(22):14506-14511.
doi: 10.1073/pnas.212525299

32. Othman SA, Soon CF, Ma NL, et al. Alginate-gelatin bioink for bioprinting of hela spheroids in alginate-gelatin hexagon shaped scaffolds. Polym Bull. 2021;78:6115-6135.
doi: 10.1007/s00289-020-03421-y

33. Li Z, Huang S, Liu Y, et al. Tuning alginate-gelatin bioink properties by varying solvent and their impact on stem cell behavior. *Sci Rep*. 2018;8(1):8020.
doi: 10.1038/s41598-018-26407-3

34. Cheng L, Yao B, Hu T, et al. Properties of an alginate-gelatin-based bioink and its potential impact on cell migration, proliferation, and differentiation. *Int J Biol Macromol*. 2019;135:1107-1113.
doi: 10.1016/j.ijbiomac.2019.06.017

35. Giuseppe MD, Law N, Webb B, et al. Mechanical behaviour of alginate-gelatin hydrogels for 3D bioprinting. *J Mech Behav Biomed Mater*. 2018;79:150-157.
doi: 10.1016/j.jmbbm.2017.12.018

36. Łabowska MB, Cierluk K, Jankowska AM, Kulbacka J, Detyna J, Michalak I. A review on the adaption of alginate-gelatin hydrogels for 3D cultures and bioprinting. *Materials (Basel, Switzerland)*. 2021;14(4):858.
doi: 10.3390/ma14040858

37. Morgan C, Inestrosa NC. Interactions of laminin with the amyloid ß peptide: implications for Alzheimer's disease. *Braz J Med Biol Res*. 2001;34:597-601.
doi: 10.1590/S0100-879X2001000500006

38. Bronfman FC, Garrido J, Alvarez A, Morgan C, Inestrosa NC. Laminin inhibits amyloid-beta-peptide fibrillation. *Neurosci Lett*. 1996;218(3):201-203.
doi: 10.1016/s0304-3940(96)13147-5

39. Rodin S, Kozin SA, Kechko OI, Mitkevich VA, Makarov AA. Aberrant interactions between amyloid-beta and alpha5 laminins as possible driver of neuronal disfunction in Alzheimer's disease. *Biochimie*. 2020;174: 44-48.
doi: 10.1016/j.biochi.2020.04.011

40. Zhang Z, Wang J, Song Y, Wang Z, Dong M, Liu L. Disassembly of Alzheimer's amyloid fibrils by functional upconversion nanoparticles under near-infrared light irradiation. *Colloids Surf B Biointerfaces*. 2019;181: 341-348.
doi: 10.1016/j.colsurfb.2019.05.053

41. Almenar-Queralt A, Falzone TL, Shen Z, et al. UV irradiation accelerates amyloid precursor protein (APP) processing and disrupts APP axonal transport. *J Neurosci*. 2014;34(9):3320-3339.
doi: 10.1523/jneurosci.1503-13.2014

42. Measey TJ, Gai F. Light-triggered disassembly of amyloid fibrils. *Langmuir*. 2012;28(34):12588-12592.
doi: 10.1021/la302626d

43. Gómez-Guillén MC, Giménez B, López-Caballero MEa, Montero MP. Functional and bioactive properties of collagen and gelatin from alternative sources: a review. *Food Hydrocolloids*. 2011;25(8):1813-1827.
doi: 10.1016/j.foodhyd.2011.02.007

44. Mancha Sánchez E, Gómez-Blanco JC, López Nieto E, et al. Hydrogels for bioprinting: a systematic review of hydrogels

synthesis, bioprinting parameters, and bioprinted structures behavior. *Front Bioeng Biotechnol*. 2020;8:776. doi: 10.3389/fbioe.2020.00776

45. Lee KY, Mooney DJ. Alginate: properties and biomedical applications. *Prog Polym Sci*. 2012;37(1):106-126. doi: 10.1016/j.progpolymsci.2011.06.003
46. Ishiwata R, Iwasa M. Cellular inertia. *Sci Rep*. 2021;11(1):23799. doi: 10.1038/s41598-021-02384-y
47. Derkach SR, Voron'ko NG, Kuchina YA, Kolotova DS. Modified fish gelatin as an alternative to mammalian gelatin in modern food technologies. *Polymers*. 2020;12(12):3051. doi: 10.3390/polym12123051
48. Kokol V, Pottathara YB, Mihelčič M, Perše LS. Rheological properties of gelatine hydrogels affected by flow-and horizontally-induced cooling rates during 3D cryo-printing. *Colloids Surf A Physicochem Eng Asp*. 2021;616:126356. doi: 10.1016/j.colsurfa.2021.126356
49. Liu S, Yang H, Chen D, et al. Three-dimensional bioprinting sodium alginate/gelatin scaffold combined with neural stem cells and oligodendrocytes markedly promoting nerve regeneration after spinal cord injury. *Regen Biomater*. 2022;9:rbac038. doi: 10.1093/rb/rbac038
50. Kaliampakou C, Lagopati N, Pavlatou EA, Charitidis CA. Alginate–gelatin hydrogel scaffolds; an optimization of post-printing treatment for enhanced degradation and swelling behavior. *Gels*. 2023;9(11):857. doi: 10.3390/gels9110857
51. Freeman FE, Kelly DJ. Tuning alginate bioink stiffness and composition for controlled growth factor delivery and to spatially direct MSC fate within bioprinted tissues. *Sci Rep*. 2017;7(1):17042. doi: 10.1038/s41598-017-17286-1
52. Chung JHY, Naficy S, Yue Z, et al. Bio-ink properties and printability for extrusion printing living cells. *Biomater Sci*. 2013;1(7):763-773. doi: 10.1039/C3BM00012E
53. Sonaye SY, Ertugral EG, Kothapalli CR, Sikder P. Extrusion 3D (bio) printing of alginate-gelatin-based composite scaffolds for skeletal muscle tissue engineering. *Materials*. 2022;15(22):7945. doi: 10.3390/ma15227945
54. Hazur J, Detsch R, Karakaya E, et al. Improving alginate printability for biofabrication: establishment of a universal and homogeneous pre-crosslinking technique. *Biofabrication*. 2020;12(4):045004. doi: 10.1088/1758-5090/ab98e5
55. Kim J, Choi YJ, Gal CW, Sung A, Park H, Yun HS. 142Development of an alginate-gelatin bioink enhancing osteogenic differentiation by gelatin release. *Int J Bioprint*. 2023;9(2):660. doi: 10.18063/ijb.v9i2.660
56. Cooke ME, Rosenzweig DH. The rheology of direct and suspended extrusion bioprinting. *APL Bioeng*. 2021;5(1):011502. doi: 10.1063/5.0031475
57. Chimene D, Kaunas R, Gaharwar AK. Hydrogel bioink reinforcement for additive manufacturing: a focused review of emerging strategies. *Adv Mater*. 2020;32(1):e1902026. doi: 10.1002/adma.201902026
58. Mancha Sánchez E, Gómez-Blanco JC, López Nieto E, et al. Hydrogels for bioprinting: a systematic review of hydrogels synthesis, bioprinting parameters, and bioprinted structures behavior. *Front Bioeng Biotechnol*. 2020;8:776. doi: 10.3389/fbioe.2020.00776
59. O'Connell C, Ren J, Pope L, et al. Characterizing bioinks for extrusion bioprinting: printability and rheology. *Methods Mol Biol*. 2020;2140:111-133. doi: 10.1007/978-1-0716-0520-2_7
60. Semba JA, Mieloch AA, Tomaszewska E, Cywoniuk P, Rybka JD. Formulation and evaluation of a bioink composed of alginate, gelatin, and nanocellulose for meniscal tissue engineering. *Int J Bioprint*. 2023;9(1):621. doi: 10.18063/ijb.v9i1.621
61. Schwab A, Levato R, D'Este M, Piluso S, Eglin D, Malda J. Printability and shape fidelity of bioinks in 3D bioprinting. *Chem Rev*. 2020;120(19):11028-11055. doi: 10.1021/acs.chemrev.0c00084
62. Cui R, Li S, Li T, et al. Natural polymer derived hydrogel bioink with enhanced thixotropy improves printability and cellular preservation in 3D bioprinting. *J Mater Chem B*. 2023;11(17):3907-3918. doi: 10.1039/D2TB02786K
63. Mouser VH, Melchels FP, Visser J, Dhert WJ, Gawlitta D, Malda J. Yield stress determines bioprintability of hydrogels based on gelatin-methacryloyl and gellan gum for cartilage bioprinting. *Biofabrication*. 2016;8(3):035003. doi: 10.1088/1758-5090/8/3/035003
64. Venkata Krishna D, Ravi Sankar M. Persuasive factors on the bioink printability and cell viability in the extrusion-based 3D bioprinting for tissue regeneration applications. *Eng Regener*. 2023;4(4):396-410. doi: 10.1016/j.engreg.2023.07.002
65. Herrada-Manchón H, Fernández MA, Aguilar E. Essential guide to hydrogel rheology in extrusion 3D printing: how to measure it and why it matters? *Gels*. 2023;9(7):517. doi: 10.3390/gels9070517
66. Tuladhar S, Clark S, Habib A. Tuning shear thinning factors of 3D bio-printable hydrogels using short fiber. *Materials (Basel, Switzerland)*. 2023;16(2):572. doi: 10.3390/ma16020572
67. Malektaj H, Drozdov AD, deClaville Christiansen JJP. Mechanical properties of alginate hydrogels cross-linked with multivalent cations. *Polymers (Basel)*. 2023;15(14):3012. doi: 10.3390/polym15143012

68. Łabowska MB, Cierluk K, Jankowska AM, Kulbacka J, Detyna J, Michalak IJM. A review on the adaption of alginate-gelatin hydrogels for 3D cultures and bioprinting. *Materials (Basel)*. 2021;14(4):858. doi: 10.3390/ma14040858

69. Shams E, Barzad MS, Mohamadnia S, Tavakoli O, Mehrdadfar AJJoBA. A review on alginate-based bioinks, combination with other natural biomaterials and characteristics. *J Biomater Appl*. 2022;37(2):355-372. doi: 10.1177/08853282221085690

70. Ioannidis K, Danalatos RI, Champeris Tsaniras S, et al. A custom ultra-low-cost 3D bioprinter supports cell growth and differentiation. *Front Bioeng Biotechnol*. 2020;8:580889. doi: 10.3389/fbioe.2020.580889

71. Leonardo M, Prajatelistia E, Judawisastra HJB. Alginate-based bioink for organoid 3D bioprinting: a review. *Bioprinting*. 2022;28:e00246. doi: 10.1016/j.bprint.2022.e00246

72. Mondal A, Gebeyehu A, Miranda M, et al. Characterization and printability of Sodium alginate-gelatin hydrogel for bioprinting NSCLC co-culture. *Sci Rep*. 2019; 9(1):19914. doi: 10.1038/s41598-019-55034-9

73. Hiller T, Berg J, Elomaa L, et al. Generation of a 3D liver model comprising human extracellular matrix in an alginate/gelatin-based bioink by extrusion bioprinting for infection and transduction studies. *Int J Mol Sci*. 2018;19(10):3129. doi: 10.3390/ijms19103129

74. Di Giuseppe M, Law N, Webb B, et al. Mechanical behaviour of alginate-gelatin hydrogels for 3D bioprinting. *J Mech Behav Biomed Mater*. 2018;79:150-157. doi: 10.1016/j.jmbbm.2017.12.018

75. Freeman FE, Kelly DJJSr. Tuning alginate bioink stiffness and composition for controlled growth factor delivery and to spatially direct MSC fate within bioprinted tissues. *Sci Rep*. 2017;7(1):17042. doi: 10.1038/s41598-017-17286-1

76. Chung JH, Naficy S, Yue Z, et al. Bio-ink properties and printability for extrusion printing living cells. *Biomater Sci*. 2013;1(7):763-773. doi: 10.1039/C3BM00012E

77. Maihemuti A, Zhang H, Lin X, et al. 3D-printed fish gelatin scaffolds for cartilage tissue engineering. *J Bioact Mater*. 2023;26:77-87. doi: 10.1016/j.bioactmat.2023.02.007

78. Derkach SR, Voron'ko NG, Sokolan NI, Kolotova DS, Kuchina YA. Interactions between gelatin and sodium alginate: UV and FTIR studies. *J Dispers Sci Technol*. 2020;41(5):690-698. doi: 10.1080/01932691.2019.1611437

79. Costa HdS, Dias MR. Alginate/bioactive glass beads: synthesis, morphological and compositional changes caused by SBF immersion method. *Mater Res*. 2021;24(4): e20200587. doi: 10.1590/1980-5373-MR-2020-0587

80. Vosough F, Barth A. Characterization of homogeneous and heterogeneous amyloid-β42 oligomer preparations with biochemical methods and infrared spectroscopy reveals a correlation between infrared spectrum and oligomer size. *ACS Chem Neurosci*. 2021;12(3):473-488. doi: 10.1021/acschemneuro.0c00642

81. Fraser PE, Nguyen JT, Inouye H, et al. Fibril formation by primate, rodent, and Dutch-hemorrhagic analogues of Alzheimer amyloid beta-protein. *Biochemistry*. 1992;31(44):10716-10723. doi: 10.1021/bi00159a011

82. Zandomeneghi G, Krebs MR, McCammon MG, Fändrich M. FTIR reveals structural differences between native beta-sheet proteins and amyloid fibrils. *Protein Sci*. 2004;13(12):3314-3321. doi: 10.1110/ps.041024904

83. Sarroukh R, Goormaghtigh E, Ruysschaert J-M, Raussens V. ATR-FTIR: A "rejuvenated" tool to investigate amyloid proteins. *Biochim Biophys Acta*. 2013;1828(10):2328-2338. doi: 10.1016/j.bbamem.2013.04.012

84. Yankner BA, Duffy LK, Kirschner DA. Neurotrophic and neurotoxic effects of amyloid beta protein: reversal by tachykinin neuropeptides. *Science (New York, NY)*. 1990;250(4978):279-282. doi: 10.1126/science.2218531

85. Mazur-Kolecka B, Golabek A, Nowicki K, Flory M, Frackowiak J. Amyloid-beta impairs development of neuronal progenitor cells by oxidative mechanisms. *Neurobiol Aging*. 2006;27(9):1181-1192. doi: 10.1016/j.neurobiolaging.2005.07.006

86. Wang X, Sun X, Gan D, et al. Bioadhesive and conductive hydrogel-integrated brain-machine interfaces for conformal and immune-evasive contact with brain tissue. *Matter*. 2022;5(4):1204-1223. doi: 10.1016/j.matt.2022.01.012

87. Pettikiriarachchi JTS, Parish CL, Shoichet MS, Forsythe JS, Nisbet DR. Biomaterials for brain tissue engineering. *Aust J Chem*. 2010;63(8):1143-1154. doi: 10.1071/CH10159

88. Sadeghi A, Afshari E, Hashemi M, Kaplan D, Mozafari M. Brainy biomaterials: latest advances in smart biomaterials to develop the next generation of neural interfaces. *Curr Opin Biomed Eng*. 2023;25:100420. doi: 10.1016/j.cobme.2022.100420

89. Bierman-Duquette RD, Safarians G, Huang J, et al. Engineering tissues of the central nervous system: interfacing conductive biomaterials with neural stem/progenitor cells. *Adv Healthc Mater*. 2022;11(7):2101577. doi: 10.1002/adhm.202101577

90. Modulevsky DJ, Cuerrier CM, Pelling AE. Biocompatibility of subcutaneously implanted plant-derived cellulose biomaterials. *PloS One*. 2016;11(6):e0157894. doi: 10.1371/journal.pone.0157894

91. Sordini L, Garrudo FFF, Rodrigues CAV, et al. Effect of electrical stimulation conditions on neural stem cells differentiation on cross-linked PEDOT: PSS films. *Front Bioeng Biotechnol*. 2021;9:591838. doi: 10.3389/fbioe.2021.591838

92. Kaur G, Adhikari R, Cass P, Bown M, Gunatillake P. Electrically conductive polymers and composites for biomedical applications. *RSC Adv*. 2015;5(47):37553-37567. doi: 10.1039/C5RA01851J

93. Jensen JB, Parmar M. Strengths and limitations of the neurosphere culture system. *Mol Neurobiol*. 2006;34(3): 153-161. doi: 10.1385/mn:34:3:153

94. Simpson LW, Szeto GL, Boukari H, Good TA, Leach JB. Collagen hydrogel confinement of Amyloid-β (Aβ) accelerates aggregation and reduces cytotoxic effects. *Acta Biomater*. 2020;112:164-173. doi: 10.1016/j.actbio.2020.05.030

95. Li YE, Jodat YA, Samanipour R, et al. Toward a neurospheroid niche model: optimizing embedded 3D bioprinting for fabrication of neurospheroid brain-like co-culture constructs. *Biofabrication*. 2020;13:015014. doi: 10.1088/1758-5090/abc1be

96. Sears NA, Seshadri DR, Dhavalikar PS, Cosgriff-Hernandez E. A review of three-dimensional printing in tissue engineering. *Tissue Eng Part B Rev*. 2016;22(4):298-310. doi: 10.1089/ten.TEB.2015.0464

97. Pillat MM, Ayupe AC, Juvenal G, et al. Differentiated embryonic neurospheres from familial Alzheimer's disease model show innate immune and glial cell responses. *Stem Cell Rev Rep*. 2023;19(6):1800-1811. doi: 10.1007/s12015-023-10542-0

98. Gaugler J, James B, Johnson T, et al. Alzheimer's disease facts and figures. *Alzheimers Dement*. 2022;18(4):700-789. doi: 10.1002/alz.12638

99. Andrade-Guerrero J, Santiago-Balmaseda A, Jeronimo-Aguilar P, et al. Alzheimer's disease: an updated overview of its genetics. *Int J Mol Sci*. 2023;24(4):3754. doi: 10.3390/ijms24043754

100. Esteve D, Molina-Navarro MM, Giraldo E, et al. Adult neural stem cell migration is impaired in a mouse model of Alzheimer's disease. *Mol Neurobiol*. 2022;59(2): 1168-1182. doi: 10.1007/s12035-021-02620-6

101. Choi YJ, Park J, Lee SH. Size-controllable networked neurospheres as a 3D neuronal tissue model for Alzheimer's disease studies. *Biomaterials*. 2013;34(12):2938-2946. doi: 10.1016/j.biomaterials.2013.01.038

102. Bernabeu-Zornoza A, Coronel R, Palmer C, Martín A, López-Alonso V, Liste I. Neurogenesis is increased in human neural stem cells by Aβ40 peptide. *Int J Mol Sci*. 2022;23(10):5820. doi: 10.3390/ijms23105820

103. Cheignon C, Tomas M, Bonnefont-Rousselot D, Faller P, Hureau C, Collin F. Oxidative stress and the amyloid beta peptide in Alzheimer's disease. *Redox Biol*. 2018;14:450-464. doi: 10.1016/j.redox.2017.10.014

104. Li F, Gong Q, Dong H, Shi J. Resveratrol, a neuroprotective supplement for Alzheimer's disease. *Curr Pharm Des*. 2012;18(1):27-33. doi: 10.2174/138161212798919075

105. Chiang MC, Nicol CJB, Lin CH, Chen SJ, Yen C, Huang RN. Nanogold induces anti-inflammation against oxidative stress induced in human neural stem cells exposed to amyloid-beta peptide. *Neurochem Int*. 2021;145:104992. doi: 10.1016/j.neuint.2021.104992

106. Walton NM, Shin R, Tajinda K, et al. Adult neurogenesis transiently generates oxidative stress. *PloS One*. 2012;7(4):e35264. doi: 10.1371/journal.pone.0035264

107. Pérez Estrada C, Covacu R, Sankavaram SR, Svensson M, Brundin L. Oxidative stress increases neurogenesis and oligodendrogenesis in adult neural progenitor cells. *Stem Cells Dev*. 2014;23(19):2311-2327. doi: 10.1089/scd.2013.0452

108. Madhavan L, Ourednik V, Ourednik J. Grafted neural stem cells shield the host environment from oxidative stress. *Ann NY Acad Sci*. 2005;1049:185-188. doi: 10.1196/annals.1334.017

109. Fonseca MB, Solá S, Xavier JM, Dionísio PA, Rodrigues CM. Amyloid β peptides promote autophagy-dependent differentiation of mouse neural stem cells: Aβ-mediated neural differentiation. *Mol Neurobiol*. 2013;48(3):829-840. doi: 10.1007/s12035-013-8471-1

110. Vázquez P, Arroba AI, Cecconi F, de la Rosa EJ, Boya P, de Pablo F. Atg5 and Ambra1 differentially modulate neurogenesis in neural stem cells. *Autophagy*. 2012;8(2):187-199. doi: 10.4161/auto.8.2.18535

111. López-Toledano MA, Shelanski ML. Neurogenic effect of beta-amyloid peptide in the development of neural stem cells. *J Neurosc*. 2004;24(23):5439-5444. doi: 10.1523/jneurosci.0974-04.2004

112. Bernabeu-Zornoza A, Coronel R, Palmer C, et al. Aβ42 peptide promotes proliferation and gliogenesis in human neural stem cells. *Mol Neurobiol*. 2019;56(6):4023-4036. doi: 10.1007/s12035-018-1355-7

113. Baglietto-Vargas D, Sánchez-Mejias E, Navarro V, et al. Dual roles of Aβ in proliferative processes in an amyloidogenic model of Alzheimer's disease. *Sci Rep*. 2017;7(1):10085. doi: 10.1038/s41598-017-10353-7

114. Micci MA, Krishnan B, Bishop E, et al. Hippocampal stem cells promotes synaptic resistance to the dysfunctional impact of amyloid beta oligomers via secreted exosomes. *Mol Neurodegener*. 2019;14(1):25. doi: 10.1186/s13024-019-0322-8

115. Wander CM, Song J. The neurogenic niche in Alzheimer's disease. *Neurosci Lett*. 2021;762:136109. doi: 10.1016/j.neulet.2021.136109

116. Jin K, Peel AL, Mao XO, et al. Increased hippocampal neurogenesis in Alzheimer's disease. *Proc Natl Acad Sci USA*. 2004;101(1):343-347. doi: 10.1073/pnas.2634794100

117. Porayette P, Gallego MJ, Kaltcheva MM, Bowen RL, Vadakkadath Meethal S, Atwood CS. Differential processing of amyloid-beta precursor protein directs human embryonic stem cell proliferation and differentiation into neuronal precursor cells. *J Biol Chem*. 2009;284(35): 23806-23817. doi: 10.1074/jbc.M109.026328

118. Matta R, Gonzalez AL. Engineered biomimetic neural stem cell niche. *Curr Stem Cell Rep*. 2019;5(3):109-114. doi: 10.1007/s40778-019-00161-2